Title Page

Next-Generation Cell-active Inhibitors of the Undrugged Oncogenic PTP4A3 Phosphatase*

John S. Lazo, Isabella K. Blanco, Nikhil R. Tasker, Ettore J. Rastelli, James C. Burnett, Sharon R. Garrott, Duncan J. Hart, Rebecca L. McCloud, Ku-Lung Hsu, Peter Wipf, and Elizabeth R. Sharlow

Department of Pharmacology (J.S.L., I.K.B., S.R.G., D.J.H., E.R.S.) and Chemistry (J.S.L., R.L.M., K-L.H.), University of Virginia, Charlottesville, VA; Department of Chemistry (N.R.T.,E.J.R., J.C.B., P.W.), University of Pittsburgh, Pittsburgh, PA

JPET Fast Forward. Published on October 10, 2019 as DOI: 10.1124/jpet.119.262188
This article has not been copyedited and formatted. The final version may differ from this version.

Running Title Page

Running Title: Iminothienopyridinedione PTP4A Phosphatase Inhibitors

Address correspondence to: John S. Lazo, Department of Pharmacology, Fiske Drug Discovery Laboratory, P.O. Box 800735, University of Virginia, Charlottesville, VA 22908-0735; Telephone: 434-243-1936; Fax: 434-982-0874; Email: lazo@virginia.edu

Text pages: 42
Tables: 3
Figures: 5
References: 43
Words in Abstract: 250
Words in Introduction: 689
Words in Discussion: 665

Abbreviations: ABC, ammonium bicarbonate; ACN**,** acetonitrile; DiFMUP, 6,8-difluoro-4-methyl-umbelliferyl phosphate; DMEM, Dulbecco's minimum essential medium; DTT, dithiothreitol; EJR-866-75, 7-imino-2-(4-(2-morpholinoethoxy)phenyl)thieno[3,2-*c*]pyridine-4,6(5*H*,7*H*)-dione; EJR-866-81, 2-(2-chlorophenyl)-7-iminothieno[3,2-*c*]pyridine-4,6(5*H*,7*H*)-dione; ESI, electrospray ionization; FASP, filter-aided sample preparation of peptides; FBS, fetal bovine serum; IAA, iodoacetic acid; IC_{50}, inhibitory concentration 50; JMS-038; 6-phenylthieno[2,3-*d*]pyrimidine-2,4(1*H*,3*H*)-dione: JMS-053, 7-imino-2-phenylthieno[3,2-*c*]pyridine-4,6(5*H*,7*H*)-dione; LC-MS/MS, liquid chromatography-tandem mass spectrometry; MALDI-TOF MS, matrix-assisted laser desorption ionization time-of-flight mass spectrometry; NRT-870-59, 7-imino-5-methyl-2-phenylthieno[3,2-*c*]pyridine-4,6(5*H*,7*H*)-dione; PBS, phosphatase buffered saline; PTP, protein tyrosine phosphatase; RFU, relative fluorescence

unit; ROS, reactive oxygen species; TBS, Tris buffered solution; Thienopyridone (7-amino-2-phenyl-5*H*-thieno[3,2-*c*]pyridin-4-one)

Section assignment:

Drug Discovery and Translational Medicine

Abstract

Oncogenic protein tyrosine phosphatases are overexpressed in numerous human cancers but they have been challenging pharmacological targets. The emblematic oncogenic PTP4A tyrosine phosphatase family regulates many fundamental malignant processes. JMS-053 (7-imino-2-phenylthieno[3,2-*c*]pyridine-4,6(5*H*,7*H*)-dione) is a novel, potent and selective PTP4A inhibitor but its mechanism of action has not been fully elucidated nor the chemotype fully investigated. Because tyrosine phosphatases are notoriously susceptible to oxidation, we interrogated JMS-053 and three newly synthesized analogs with specific attention on the role of oxidation. JMS-053 and its three analogs were potent *in vitro* PTP4A3 inhibitors, but 7-imino-5-methyl-2-phenylthieno[3,2-*c*]pyridine-4,6(5*H*,7*H*)-dione (NRT-870-59) appeared unique among the thienopyridinediones with respect to its inhibitory specificity for PTP4A3 versus both a PTP4A3 A111S mutant and an oncogenic dual specificity tyrosine phosphatase CDC25B. Like JMS-053, NRT-870-59 was a reversible PTP4A3 inhibitor. All of the thienopyridinediones retained cytotoxicity against human ovarian and breast cancer cells grown as pathologically-relevant three-dimensional spheroids. Inhibition of cancer cell colony formation by NRT-870-59, like JMS-053, required PTP4A3 expression. JMS-053 failed to generate significant detectable reactive oxygen species *in vitro* or in cancer cells. Mass spectrometry results indicated no disulfide bond formation nor oxidation of the catalytic Cys104 after *in vitro* incubation of PTP4A3 with JMS-053 or NRT-870-59. Gene expression profiling of cancer cells exposed to JMS-053 phenocopied many of the changes seen with the loss of PTP4A3 and did not indicate oxidative stress. These data demonstrate that PTP4A phosphatases can be selectively targeted with small molecules that lack prominent reactive oxygen species generation and encourage further studies of this chemotype.

Significance Statement

Protein tyrosine phosphatases are emerging as important contributors to human cancers. We report on a new class of reversible protein phosphatase small molecule inhibitors that are cytotoxic to human ovarian and breast cancer cells, do not generate significant reactive oxygen species *in vitro* and in cells, and could be valuable lead molecules for future studies of PTP4A phosphatases.

Introduction

The PTP4A (also known as PRL) phosphatases are a unique subfamily of protein tyrosine phosphatases (PTPs) comprising three highly homologous members (PTP4A1, PTP4A2, and PTP4A3) with ~80% amino acid sequence identity. PTP4A3, and to a lesser extent PTP4A1 and PTP4A2, are overexpressed in many types of cancer, promote tumor invasion and dissemination, and contribute to poor patient prognosis (Daouti et al., 2008; den Hollander et al., 2016). The PTP4A family members have been categorized among the most oncogenic of all phosphatases and, consequently, they represent attractive cancer therapeutic targets (Yu and Zhang, 2017). Like almost all of the other PTPs, however, the PTP4A family members lack readily available potent and selective small molecule inhibitors and are even thought by some investigators to be undruggable (Lazo and Sharlow, 2016; Stanford and Biottini, 2017). This notion has been sustained because PTPs are intracellular and the phosphorylated substrates are highly charged, making it difficult for mimics of the substrates to reach the phosphatase. There is also considerable amino acid conservation in the active site of many PTPs. Nonetheless, we previously synthesized JMS-053 (7-imino-2-phenylthieno[3,2-*c*]pyridine-4,6(5*H*,7*H*)-dione) and discovered its potent and reversible PTP4A3 inhibitory profile (Salamoun et al., 2016; McQueeney et al., 2017). We documented that JMS-053 inhibited cancer cell migration and spheroid growth *in vitro*, attenuated *in vivo* ovarian tumor growth, and mitigated the disruption of the microvascular endothelial barrier function by vascular endothelial growth factor or lipopolysaccharide (McQueeney et al., 2017; McQueeney et al., 2018). The current project was designed to probe the structural features of JMS-053 that contribute to PTP4A3 inhibition and to investigate further the mechanism of enzyme inhibition.

The generation of reactive oxygen species (ROS) is an intrinsic component of endogenous growth factor stimulation and metabolism, which has fortified the hypothesis that protein oxidation is a post-translational modification involved in normal cell signaling and gene expression (Chakraborty et al., 2019). This suggests manipulation of ROS could be a valuable approach for the treatment of cancer. Indeed, cancer cells are known to produce more ROS than non-transformed cells (Schieber and Chandel, 2014) and at least 12 clinically used anticancer drugs either directly or indirectly generate ROS (Yokoyama et al., 2017). Recent studies have shown that many proteins become oxidized at cysteine residues under conditions that increase intracellular ROS levels (van der Reest et al., 2018). Several classes of attractive therapeutic targets are susceptible to ROS-mediated inactivation, including metalloenzymes, cysteine proteases and PTPs, because they contain a cysteine in their active site, which is readily deprotonated as a consequence of the surrounding peptide side chain functionality (Pani et al., 2000; Johnston et al., 2008). The catalytic thiol can be oxidized to a metastable sulfenic acid and further oxidized to sulfinic or sulfonic acid, which are considerably more stable under physiological conditions. Other inactivating oxidation processes have also been reported with PTPs. For example, PTEN, CDC25, LMW-PTP, DUSP12, DUSP6, SHP1, SHP2, LYP and PTP4A phosphatases are susceptible to intramolecular disulfide bond formation (Bonham and Vacratsis, 2009; Tanner et al., 2011; Ishii et al., 2013). The creation of cyclic sulfenylamide bonds (Defelipe et al., 2015) and degradation of the catalytic cysteine to a glycine have been detected in PTPs (Orsatti et al., 2009). Such observations raise the question whether small molecules that generate oxidative stress could promote these types of post-translational modifications and, thus, inactivate PTPs.

Although *in vitro* PTP4A3 inhibition by JMS-053 is reversible, we previously did not formally exclude the possibility that JMS-053 forms ROS, which is a common deactivation process found for other PTP inhibitors (Johnston et al., 2008). Previous work indicates disulfide bond formation is reversible as is sulfenic acid oxidation of the catalytic thiol (Orsatti et al., 2009; Ishii et al., 2013). Thus, in the current report, we investigated the ability of JMS-053 and several recently synthesized analogs of JMS-053 to generate ROS and to inhibit PTP4A family members. We also biochemically tested our previously described computational models of the interactions between JMS-053 and PTP4A3 (McQueeney et al., 2017; Tasker et al., 2019) and interrogate the cytotoxicity of the JMS-053 analogs to human and mouse cancer cells to further clarify the actions of these compounds as chemical biology tools.

Materials and Methods

Compounds and reagents. Thienopyridone (7-amino-2-phenyl-5*H*-thieno[3,2-*c*]pyridin-4-one), DA-3003-1 (6-chloro-7-(2-morpholin-4-yl-ethylamino)-quinoline-5-8-dione), JMS-053, the inactive control compound JMS-038 (6-phenylthieno[2,3-*d*]pyrimidine-2,4(1*H*,3*H*)-dione), EJR-866-75 (7-imino-2-(4-(2-morpholinoethoxy)phenyl)thieno[3,2-*c*]pyridine-4,6(5*H*,7*H*)-dione), EJR-866-81 (2-(2-chlorophenyl)-7-iminothieno[3,2-*c*]pyridine-4,6(5*H*,7*H*)-dione), and NRT-870-59 (7-imino-5-methyl-2-phenylthieno[3,2-*c*]pyridine-4,6(5*H*,7*H*)-dione) (Fig. 1) were synthesized as previously described (Brisson et al., 2005; Salamoun et al., 2016; Tasker et al., 2019). DiFMUP was purchased from ThermoFisher Scientific (Waltham, MA). Dimethyl sulfoxide (DMSO) was obtained from VWR (Radnor, PA). All other reagents were obtained from Sigma-Aldrich (St. Louis, MO) unless otherwise indicated.

pET15b bacterial expression constructs. pET15b-His_6-PTP4A3, -PTP4A3-K144I, -PTP4A3-C49S, -PTP4A3-A106V, -PTP4A3-A111S, -PTP4A1, -PTP4A2, -CDC25B1 and -DUSP3 bacterial expression constructs were obtained from Genscript (Piscataway, NJ). Recombinant human proteins were expressed and purified using previously described procedures (McQueeney et al., 2017; McQueeney et al., 2018).

Cancer cell lines. Authenticated OVCAR4 cells were obtained from Charles River Laboratories (New York, NY) and Kuramochi from (Sekisui XenoTech, LLC, Kansas City, KS). Authenticated MDA-MB-231, Hs578T, and IMR90 cells were obtained from the America Type Culture Collection (Manassas, VA). Nonmalignant human H10-180 ovarian epithelial cells were a gift from Charles N. Landen (University of Virginia) and previously described (McQueeney et al.,

2017; McQueeney et al., 2018). OVCAR4, Kuramochi, and MDA-MB-231 cells were maintained in RPMI (Life Technologies, Grand Island, NY) supplemented with 10% fetal bovine serum (FBS), with no antibiotics, and were passaged <20 times. Hs578T cells were grown in DMEM supplemented with 10% FBS and 0.01% bovine insulin, with no antibiotics, and were likewise passaged <20 times. The four human cell lines are valuable because they are genetically diverse and have been fully annotated for mutations and mRNA expression by the Cancer Cell Line Encyclopedia (https://portals.broadinstitute.org/ccle). All four cell lines have mutations in DNA binding domain of TP53 (Supplemental Table 1), which encodes the direct target of PTP4A3: p53 (Basak et al., 2008). Each of the cell lines also have missense mutations in HRAS, KRAS, or IL6R, which could influence the actions of PTP4A3 (Supplemental Table 1). Mixed mouse PTP4A3 wildtype and null colon cancer cells and the colony formation assay conditions were previously described (McQueeney et al., 2018). Exponentially growing ovarian and breast cancer cells were harvested and seeded (250 cells/22 µL) in each well of a 384 well ultralow attachment U-bottom microtiter plate (Corning, Corning, NY). Plates were incubated for 24 h (37^{o} C at 5% CO_2) to allow for spheroid formation. Compounds (3 µL) were then added in final DMSO concentrations of 0.5%, as was the vehicle control (0.5% DMSO). Positive control wells contained 10% DMSO. The microtiter plates were incubated for 48 h (37° C, 5% CO_2) and 25 µL of the CellTiterGlo 3D reagent (Promega, Fitchburg, WI) were added. Plates were incubated with shaking for 30 min at room temperature. Luminescence data were captured on a SpectraMax M5 multimode plate reader. The effects of NRT-870-059 on colon cancer colony formation were performed as previously described (McQueeney et al., 2018).

***In vitro* biochemical analysis of PTP4A inhibition.** Enzyme activity assays were performed in triplicate in 384-well Greiner Bio-One black small volume microtiter plates, as previously

JPET Fast Forward. Published on October 10, 2019 as DOI: 10.1124/jpet.119.262188
This article has not been copyedited and formatted. The final version may differ from this version.

described (Salamoun et al., 2016), using recombinant human His_6-tagged PTP4A1, PTP4A2, PTP4A3, PTP4A3 mutants, CDC25B, or DUSP3 and substrate DiFMUP (12 μM) incubated at 25°C for 25 min in 40 mM Tris-HCl (pH 7.0), 75 mM NaCl, 2 mM EDTA, and 4 mM dithiothreitol (DTT) buffer. Enzyme activity assays were performed in triplicate in 384-well Greiner Bio-One black small volume microtiter plates, as previously described (McQueeney et al., 2017; McQueeney et al., 2018), using recombinant human His_6-tagged PTP4A1, PTP4A2, PTP4A3, PTP4A3 mutants, CDC25B, or DUSP3 and substrate DiFMUP (12 μM) incubated at 25°C for 25 min in 40 mM Tris-HCl (pH 7.0), 75 mM NaCl, 2 mM EDTA, and 4 mM dithiothreitol (DTT) buffer. The assay was fully automated using an Agilent Bravo Liquid Handling Platform and miniaturized to 15 µL total volume. Dilutional reversibility assays were performed in a 100 µL total reaction volume using the same assay conditions (McQueeney et al., 2017; McQueeney et al., 2018). His_6-tagged PTP4A3 (1 µg) was pre-incubated for 30 min with 0, 86 or 860 nM compound and then diluted to 10-fold. Reactions were initiated with the addition of 45 µL of substrate for a final DiFMUP concentration of 12 µM and incubated at room temperature for 25 min. Pre-incubation studies with NRT-870-59 were performed by incubating the compound with PTP4A3 for 2 h with continuous shaking after which time substrate was added and the standard assays conditions followed. Fluorescence data was captured on a SpectraMax M5 (San Jose, CA) and phosphatase activity was expressed as a percent maximal activity.

***In vitro* and cell-based reactive oxygen species assessments.** *In vitro* generation of ROS by JMS-053 and it analogs was determined by two orthogonal fluorescence- and absorbance-based assays using resazurin and phenol red as substrates, respectively, as described previously (Lor et al., 2007; Johnston, 2011). Cellular ROS generation was determined using

ROS-Glo H_2O_2 assay (Promega, Madison, WI) according to manufacturer's instructions. In brief, one thousand OVCAR4 cells were seeded per well of a 384-well microtiter plate and incubated until they were ~70% confluent. Cells were exposed to compounds and controls for 10 min then ROS-Glo Detection Solution was added to each well. Plates were incubated for 20 min and relative luminescence units were captured on a SpectraMax M5.

Filter-aided sample preparation of peptides for LC-MS/MS analysis. Samples were prepared in duplicate using a modified FASP protocol (Wisniewski et al., 2009) to compare between reducing vs. non-reducing conditions. Purified PTP4A3 (30 µg) was incubated with 200 nM of JMS-053, NRT-870-59 or water for 10 min at room temperature. Once the incubation was complete, samples were diluted in either 10 M urea/25 mM ammonium bicarbonate (ABC) or 2 mM urea in Tris-HCl, transferred to 10 kDa filters (Sartorious, AG, Göttingen, Germany) and centrifuged at 14,000 x g for 15 min. Samples were diluted in buffer and centrifuged two more times before further treatment, all flow through was discarded. Reduction with 12.5 mM DTT was performed in samples denatured by the urea/ABC buffer for 45 min at 56º C followed by alkylation at 37º C with 50 mM iodoacetic acid (IAA) in the dark, while corresponding samples were alkylated with 2 mM IAA at 37º C in the dark for 2 h. All filters were subsequently washed with urea/ABC buffer and centrifuged three times at 14,000 x g for 15 min. This step was repeated another three times with 25 mM ABC before the proteolytic digest. Filters were transferred to new tubes before the addition of trypsin/lys-c (Promega) at a 1:100 ratio of protease to PTP4A3 and incubated in a shaker at 37º C for 12 h. Filter units were transferred to new, low-bind, tubes washed with 25 mM ABC and centrifuged three times at 14,000 x g for 10 min. The flow through was collected and acidified with 0.1% formic acid, desalted on C18

StageTips, and lyophilized. Peptides were re-suspended in 50 µL of 0.1% formic acid for analysis.

ESI LC-MS/MS acquisition. An integrated autosampler-LC (Easy-nLC 1200, ThermoFisher Scientific, Waltham, MA) was used to load peptides onto a trap column (Nano-Trap, Thermo Fisher Scientific, 2 cm, 5 µm C18) and washed for 2 min with 1% B (80% acetonitrile (ACN), 1% formic acid). The peptides were eluted from the trap column and through a homemade nanocapillary analytical column (10 cm, 5 µm C18 packed in 360 µm o.d. x 75 µm i.d. fused silica), with an integrated electrospray tip, using a 65 min 1-95% reverse-phase LC gradient (A: 0.1% formic acid; B: 80% ACN, 0.1% formic acid) with the following parameters: 0-2 min 1% B, 400 nL/min; 2-21 min to 45% B, 300 nL/min; 21-25 min 95% B, 300 nL/min; 25-35 min, 1% B, 400 nL/min. The eluting peptides were analyzed using a linear ion trap mass spectrometer (ThermoFisher Scientific), which was operated with a top 5 data-dependent acquisition method that consisted of one full MS1 scan (375 - 1,800 *m/z*) followed by 5 MS2 scans of the most abundant ions with a normalized collision energy of 35. Peptide identification as accomplished by matching observed peptide *m/z* values to predicted average peptide masses for PTP4A3 by using an ExPASy *in silico* digest (PeptideMass) with a 500 ppm mass tolerance (Gasteiger et al., 2005). Peptides were further verified by matching fragment ions predicted from the sequence using ProteinProspector MS-Product (v 5.22.1).

Gene expression. Total RNA was isolated from previously described (McQueeney et al., 2018) wildtype PTP4A3 mouse colon cancer cells treated with 1 µM JMS-053 or vehicle-control (1% DMSO) for 24 h or isogenic PTP4A3 null mouse colon cancer cells. Next-Gen sequencing was conducted as previously described (McQueeney et al., 2018) and pathway analyses were

conducted with transcripts that were either significantly increased or decreased using Reactome software (https://reactome.org). Total RNA was extracted from human and mouse cells to measure PTP4A3 mRNA levels by real-time quantitative polymerase chain reaction and normalized to human GAPDH, actin, and HPRT as previously described (McQueeney et al., 2018).

Statistical analysis. All statistical analyses were performed with GraphPad Prism 7.0. Data are presented as average (mean) ± SD or SE. P values were calculated with Student's *t* test for comparisons involving two groups or one-way or two-way ANOVA for comparisons involving >two groups. $P<0.05$ was considered statistically significant. Each experiment is represented by at least three biological replicates and three technical replicates (per independent experiment) unless otherwise indicated.

JPET Fast Forward. Published on October 10, 2019 as DOI: 10.1124/jpet.119.262188
This article has not been copyedited and formatted. The final version may differ from this version.

Results

Inhibition of PTP4A3 by JMS-053 and new analogs. We recently synthesized a series of 19 analogs of the novel iminothienopyridinedione JMS-053, which is a reversible, allosteric, and cell-active small molecule PTP4A3 inhibitor with an *in vitro* IC_{50} for recombinant human PTP4A3 of ~30 nM (Salamoun et al., 2016; McQueeney et al., 2017; McQueeney et al., 2018; Tasker et al., 2019). From the series, three JMS-053 analogs, EJR-866-75, EJR-866-81, and NRT-870-59 (Fig. 1), were selected for further study, because they retained the ability to potently inhibit PTP4A3 *in vitro* and had structural features that potentially should reduce metabolism or increase water solubility (Tasker et al., 2019). We also synthesized the valuable inactive congener JMS-053 (Fig. 1) as a control compound. Since the endogenous substrate for PTP4A3 has not yet been firmly established, previous enzymatic studies employed artificial small molecule substrates, such as 6,8-difluoro-4-methylumbelliferyl phosphate (DiFMUP). With this substrate, PTP4A3 utilizes a two-step *in vitro* kinetic cycle, which involves a long-lived phosphocysteine intermediate (Gulerez et al., 2016). The first step is rapid followed by a slower steady-state conversion, which is likely to represent the kinetically more meaningful parameter within cells. Using DiFMUP and a 25 min incubation that reflects the steady-state rate, we found that the PTP4A3 IC_{50} for EJR-866-75, ERJ-866-81, and NRT-870-59 was 98.2, 36.1, and 86.0 nM, respectively (Table 1, Supplemental Fig. 1). The inactive control congener, JMS-038, failed to inhibit PTP4A3 (Table 1, Supplemental Fig. 1). JMS-053 was equipotent against PTP4A3 and its close family members PTP4A1 and PTP4A2, confirming our previous results (McQueeney et al., 2017) (Table 1, Fig. 2A). This pan-PTP4A phosphatase inhibition was also observed with a less potent parent compound, thienopyridone (Daouti et al., 2008; Hoeger et al., 2014). ERJ-866-75 showed little preference among the PTP4A family members (Table 1, Fig. 2B). Surprisingly, EJR-866-81 and the thienopyridone core modified NRT-870-59 displayed an even

more pronounced preference for PTP4A3 compared to PTP4A2 (Table 1, Fig. 2C-D). This is the first demonstration of tractable selectivity by a potent small molecule inhibitor for PTP4A3 versus PTP4A2, which is rather remarkable considering there is ~80% identity in the overall amino acid composition between these two phosphatases and 100% identity in the catalytic P loop (HCVAGLGRA) (Rios et al., 2012). It is noteworthy, however, that a 10-fold selectivity for inhibition of PTP4A1 over PTP4A3 was previously reported for the chemically unrelated procyanidin B3 (Stadlbauer et al., 2015). JMS-038 was inactive against all three PTP4A3 family members (Fig. 2E).

Inhibition specificity with other PTPs. JMS-053 inhibited the oncogenic dual specificity phosphatase CDC25B with an IC_{50} of 92.6 nM (Table 1, Supplemental Fig. 2A), consistent with our previous report (McQueeney et al., 2017). EJR-866-81 and EJR-866-75 also were potent *in vitro* inhibitors of CDC25B with IC_{50} values of 65.5 and 122.6 nM, respectively (Table 1, Supplemental Fig. 2B-C). In contrast, NRT-870-59 did not inhibit CDC25B at concentrations $\leq$1 μM (Table 1, Supplemental Fig. 2D). All of the compounds were 5-6-fold less potent as inhibitors of the dual specificity phosphatase DUSP3 (Table 2). Like JMS-053 (McQueeney et al., 2017), NRT-870-59 inhibition was reversible as measured with a dilutional assay (Fig. 2F).

Inhibition of PTP4A3 mutants. We previously proposed a binding site for JMS-053 based on computational docking studies using an energy refined structure (McQueeney et al., 2017). In agreement with a noncompetitive mechanism, the putative allosteric binding site occupied a pocket that was flanked by the α3, α4, and α6 helices on PTP4A3 along with the WPD loop. The well-desolvated inhibitor binding mode was predicted to hold the WPD loop in the closed conformation in part via hydrogen bonds between the compound's pyridinedione oxygens and

the K144 side chain amine (McQueeney et al., 2017). We tested this model by generating the PTP4A3 K144I mutant, which we predicted would be resistant to inhibition by JMS-053. The K144I mutant shared a similar steady state K_m and K_{cat} for the artificial substrate DiFMUP (4.73 μM and 6.47 min^{-1}) with wildtype PTP4A3 (4.04 μM and 5.77 min^{-1}) (Table 2, Supplemental Fig. 3A) and was inhibited with a similar IC_{50} by JMS-053 (42.7 $\pm$ 8.0 nM) (Table 1, Supplemental Fig. 3B). These results suggested that K144 was not essential for JMS-053 binding to PTP4A3. The IC_{50} for EJR-866-81, EJR-866-75, and NRT-870-59 were also similar for the K144I mutant and wildtype, while JMS-038 did not inhibit the mutant form of PTP4A3 (Table 1, Supplemental Fig. 3C-F). Thus, we further modified our exploratory docking model with the A chain of PTP4A3 PDB entry 5TSR, which represents the reduced form of the enzyme with a closed WPD loop and proposed strong hydrogen bond interactions with JMS-053 to A106 and A111 (Tasker et al., 2019). We created the A106V and A111S mutants to test this hypothesis. The A106V mutant exhibited a markedly higher K_m for DiFMUP and a significantly lower K_{cat}/K_m compared to the wildtype PTP4A3 (Table 2). This finding would be consistent with the proposed role of the flexible WPD loop. JMS-053 and all three analogs, however, retained similar IC_{50} values compared to the wildtype enzyme. These results suggested an interaction with A106 was not essential for JMS-053 inhibition of PTP4A3. In contrast, the A111S mutant had a K_{cat}/K_m that was similar to the wildtype enzyme, although the mutant K_m and K_{cat} values were both higher than that of the wildtype enzyme. The IC_{50} values for JMS-053, EJR-866-81, EJR-866-75, and NRT-870-59 were higher for the A111S mutant compared to the wildtype phosphatase (Table 1, Supplemental Fig. 4), supporting a role for this amino acid in the binding and inhibition of this class of compounds.

JPET Fast Forward. Published on October 10, 2019 as DOI: 10.1124/jpet.119.262188
This article has not been copyedited and formatted. The final version may differ from this version.

Many PTPs are inhibited by intramolecular disulfide bond formation (Buhrman et al., 2005; Ishii et al., 2013) and C49 has been reported to be the only cysteine involved in an intramolecular disulfide bond formation with the catalytic C104 of PTP4A3 (Kozlov et al., 2004; Orsatti et al., 2009). Therefore, we generated the conservative C49S PTP4A3 mutant, which had impaired catalytic activity consistent with previous published results (McParland et al., 2011; Zhang et al., 2017) (Table 2, Supplemental Fig. 5). PTP4A3 C49S also had a 10-fold higher steady state K_m for DiFMUP in agreement with previous results with a different artificial substrate (Kozlov et al., 2004) but a similar K_{cat} compared to wild type PTP4A3 (Table 2). The higher K_m likely reflects the importance of the CXnE motif in PTP4A3 for DiFMUP dephosphorylation, although it is interesting to note that previous work demonstrates mutation of the glycine adjacent to C49, namely E50R, does not alter the K_m of PTP4A3 for DiFMUP but increases the K_{cat} (Hoeger et al., 2017). JMS-053 and all of the analogs, with the exception of the inactive JMS-038 control compound, retained partial inhibition of PTP4A3 C49S (Table 1, Supplemental Fig. 5). Thus, C49-C104 disulfide bond formation is unlikely to be the primary inhibitory mode of JMS-053 or the analogs, although these data did not formally exclude the involvement of C49. We previously hypothesized (McQueeney et al., 2017) that JMS-053 interacted with an allosteric site flanked by the highly flexible WPD loop and the α3 helix, which are located close to C49. This binding mode may account for the partial inhibition of the C49S mutant by JMS-053 and its analogs.

Reactive oxygen species generation. Many small molecule PTP inhibitors have been found to be redox cycling compounds, generating H_2O_2, superoxide, hydroxyl radicals and singlet oxygen in the presence of strong reducing agents, such as DTT, that are common in many PTP assay buffers (Soares et al., 2010; Johnston, 2011). Therefore, we formally examined JMS-053 and its

analogs for their ability to generate ROS in the *in vitro* buffer conditions (Fig. 3). DTT can cause a net $2e^-$ reduction of resazurin to create the highly fluorescent product resorufin and this reaction forms the basis of a successfully used assay to identify redox cycling compounds particularly those that generate H_2O_2 in high throughput screening assays (Lor et al., 2007; Johnston, 2011). A positive control quinolinedione DA-3003-1, which we previously found generates ROS *in vitro* with PTP assay buffers (Vogt et al., 2008), yielded a concentration-dependent increase in the resorufin oxidized product, as measured by relative fluorescence units (RFU). Concentrations of DA-3003-1 as low as 15 nM caused a significant increase in oxidized product (Fig. 3A). In contrast, the JMS-053 series show little or no ability to form ROS at concentrations that two-fold higher than the IC_{50}, i.e., <62 nM, when compared to the inactive compound JMS-038. We also evaluated the redox liabilities of JMS-053 and its analogs using a phenol red-horseradish peroxidase assay, which can readily detect H_2O_2 generated *in vitro* by redox cycling compounds co-incubated with DTT and is based on absorbance not fluorescence (Vogt et al., 2008). The positive control compound DA3003-1 (Vogt et al., 2008) produced a pronounced concentration-dependent increase in absorbance while no change in absorbance was detected with JMS-053, EJR-866-75, NRT-870-59 and JMS-038 at concentrations ≤50 μM (Fig. 3B). EJR-866-81 showed no evidence for H_2O_2 generation at concentrations of ≤25 μM but increased absorbance at 50 μM (Fig. 3B). Moreover, preincubation of PTP4A3 with JMS-053 for 2 h did not markedly alter PTP4A3 inhibition (Fig. 3C), consistent with our previous observation of reversibility (McQueeney et al., 2017). Addition of 1 U/mL of catalase decreased by 19-fold the IC_{50} of the control ROS-generating compound DA-3003-1 from 60.2 nM to 1.1 μM, while the same catalase concentration only decreased the IC_{50} of JMS-053 by 3-fold to 108.5 nM. The modest reduction in the JMS-053 IC_{50} in the presence of catalase might reflect the production of

low levels of ROS that were not detected with the surrogate assays or simply be due to binding of the compound to catalase. This aspect of the work is worthy of further investigation.

Lack of PTP4A3 oxidation as measured by mass spectrometry. Although the bulk of our assays provided no support for significant ROS generation by JMS-053 and its analogs, the kinetics and chemistry of ROS are notoriously complex. Therefore, we used liquid chromatography-tandem mass spectrometry (LC-MS/MS) combined with selective Cys alkylation to examine the status of the disulfide forming between C104 and C49, which forms the functionally important CX_nE motif. PTP4A3 was incubated in the presence or absence of 200 nM JMS-053 for 30 min and then labeled at reduced Cys residues, using the alkylating reagent iodoacetamide. After alkylation, the samples were digested with TPCK-modified trypsin/lys-c and the trypic digests were analyzed by electrospray ionization (ESI) LC-MS/MS as previously described (Orsatti et al., 2009). Prominent peaks for each of the Cys-containing peptides were observed, and there was no evidence for C49-C104 dimer formation in the absence or presence of JMS-053 (Fig. 4). Moreover, JMS-053 did not appear to oxidize C49, C93 or C104, convert the catalytic C104 to glycine, or generate a sulfenyl-amide species (Fig. 4). No cysteine oxidation was observed with a pre-incubation of PTP4A3 and NRT-870-59 in the absence or presence of DTT (Supplemental Fig. 6). Collectively, these data further support an inhibitory mechanism that is independent of the generation of ROS.

Cytotoxicity of JMS-053 and analogs to cancer cells. We next investigated the ability of the JMS-053 series to kill human tumors cells grown as 3-dimensional spheroids, which retain many of the critical intercellular signaling pathways that are modified by PTP4A3 (McQueeney et al., 2018). We used four human cancer cell lines with diverse genetic backgrounds that have been

well annotated in the publicly available Cancer Cell Line Encyclopedia (https://portals.broadinstitute.org/ccle). All four cell lines have higher PTP4A3 expression levels compared to a nonmalignant counterpart (Supplemental Figure 7A-B). Human triple negative breast cancer Hs578T and high grade serous ovarian cancer OVCAR4 cells were the most sensitive to a brief 48 or 72 h exposure to JMS-053 with IC_{50} values <9 μM, while the high grade serous ovarian Kuramochi cells, which have a long doubling time (~72 h), had an intermediate potency and triple negative MDA-MB-231 breast cancer cells were the least sensitive (Table 3, Supplemental Fig. 8). This profile of Hs578T and OVCAR4 being most responsive was seen with all analogs. EJR-855-81, EJR-866-75, and NRT-870-59 were cytotoxic to human Hs578T breast cancer and OVCAR4 ovarian cancer spheroid tumor cells grown *in vitro* with IC_{50} values below 20 μM. Spheroid colony formation is an alternative method to evaluate extracellular matrix-dependent cytotoxicity. Similar to our previous results with JMS-053 (McQueeney et al., 2017), wild type mouse colon cancer cells, which express considerable PTP4A3 (Supplemental Fig. 7C) (McQueeney et al., 2017), exhibited a statistically significant decrease in colony formation after exposure to 500 nM NRT-870-59 with a somewhat flat concentration-response curve up to 5 μM. Importantly, however, no statistically significant decrease in colony formation was observed with the PTP4A3 null cells treated at any concentration of NRT-870-59 and no difference in colony formation was seen between wild type and null cells treated with 5 μM NRT-870-59 (Fig. 5A), indicating a dependence for target expression for the cellular effects. This is similar to what we previously observed with JMS-053 (McQueeney et al., 2017). The low colony numbers with our vehicle treated PTP4A3 null cells does, however, limit the dynamic range of the assay.

Lack of cellular ROS formation with JMS-053. We next probed the potential of JMS-053 and its analogs to generate significant ROS bursts within cells. A robust elevation of ROS was observed 10 min after exposure to the positive control DA-3003-1 (Fig. 5B). In contrast, neither JMS-053 nor any of the analogs produced detectable ROS in cells (Fig. 5B). This lack of intracellular ROS generation coupled with the known endogenous reductants of the PTP4A3 disulfide bond, such as thioredoxin-related protein 23 (Ishii et al., 2013), offers further support for an oxidant-independent mechanism of inhibition by JMS-053 and its analogs. The oxidant independence of JMS-053 was further supported by examining the changes in gene expression, which have been extensively analyzed by others using H_2O_2 (Harris et al., 2019). When we compared the mRNA expression of 31,037 genes in a previously described isogenic pair of colorectal cancer cells that are wildtype or null for PTP4A3 (McQueeney et al., 2018), we detected 3,289 transcripts that were differentially expressed in wild type and null cells. A pathway analysis of these up and down regulated gene transcripts implicated extracellular matrix and ERK pathway alterations but not oxidative stress (Supplemental Fig. 9A). None of the gene transcripts commonly associated with oxidative stress, such as NRF2, NQO1, HMOX1, HSPA6, GADD34, or CHOP (Harris et al., 2019), were elevated in the PTP4A3 null cells. Treatment of the wildtype colorectal cancer cells for 24 h with 1 μM JMS-053 did not elevate the transcripts commonly associated with oxidative stress, such as NRF2, NQO1, HMOX1, HSPA6, GADD34, or CHOP. A pathway analysis of the up and down regulated gene transcripts did not demonstrate any prominent changes in the canonical oxidative stress pathways (Supplemental Fig. 9B). The pathways common to the expression of the 241 gene transcripts altered in both the null cells and the JMS-053 treated wildtype cells were frequently related to extracellular matrix and migration including hemidesmosome assembly, laminin interactions, anchoring fibril formation, keratinization, glycosaminoglycan synthesis, and O-glycosylation (Fig. 5C). This is

consistent with our previous observations about the importance of the extracellular matrix and adhesion in the cellular actions of PTP4A3 (McQueeney et al., 2018). These changes could be related to the proposed role of PTP4A3 in regulating epithelial mesenchymal transition (Wang et al., 2007) and the keratins in colon cancer (Karantza, 2011). These subjects warrant further investigation.

JPET Fast Forward. Published on October 10, 2019 as DOI: 10.1124/jpet.119.262188
This article has not been copyedited and formatted. The final version may differ from this version.

Discussion

A number of cellular functions have been attributed to PTP4A3 family members (Rios et al., 2012; Yu and Zhang, 2017; Hardy et al., 2018). Most but not all of the evidence supporting the oncogenic roles of PTP4A3 have been generated using genetic approaches, which are not easily titratable and frequently irreversible. Therefore, rigorously validated small molecules that inhibit PTP4A phosphatases should be valuable pharmacological reagents. While this manuscript was being prepared, work was published suggesting thienopyridone and JMS-053 generated ROS and the authors concluded that these compounds were inappropriate for therapeutic development or studies of PTP4A function (Zhang et al., 2019). Based on our results, however, we must demur. We found reversible inhibition with dilution assays, which would be inconsistent with the formation of a sulfinic or sulfonic at cysteines and would be expected from extreme oxidation by ROS. While the authors reported NMR results that indicated a conformation change consistent with disulfide bond formation between C49 and C104 in PTP4A3 (Zhang et al., 2019), we observed no evidence for disulfide bond formation by LC-MS/MS with either JMS-053 or NRT-870-059 (Fig. 4 and Supplemental Fig. 6). Importantly, we did not observe ROS formation in cells treated with JMS-053 (Fig. 5B) nor did we find a change in the gene expression profile consistent with oxidative stress (Fig. 5C).

There are several significant differences between the our study and that of Zhang *et al.* (Zhang et al., 2019), which might explain the disagreement in the conclusions. First, we examined steady-state kinetics, which we believe are more pharmacologically relevant, rather than burst kinetics with an artificial substrate. Second, we employed control compounds, the inactive JMS-038 and the ROS generating compound DA-3003-1, in most of our studies. Third, we examined the reduction of resorzurin *in vitro* with JMS-053 at ≤125 nM or 5 x IC_{50} values

rather than with 5 μM, which is 160-fold greater than the IC_{50} value for PTP4A3. Fourth, we avoided using high concentrations of the solvent DMSO, which we have found facilitates PTP4A3 oxidation *in vitro*. Fifth, we used full-length recombinant PTP4A3 rather than a truncated version of the phosphatase. Finally, we extensively interrogated the purity of our compounds with ^{1}H and ^{13}C NMR, crystallography, LC/MS, and elemental analyses and we did not rely solely on ^{1}H NMR to document compound purity. Indeed, a comparison between our published ^{1}H NMR (Salamoun et al., 2016; Tasker et al., 2019) and that used in the previously published work (Zhang et al., 2019) suggests considerable impurities or decomposition of the compounds used in the Zhang *et al*. study (Zhang et al., 2019). PTP4A3 is notoriously susceptible to oxidation from cations and oxidized DMSO (Orsatti et al., 2009) so great care needs to be taken in the preparation of PTP4A3, the buffers, and the compound being tested.

Thus, we propose that the iminothienopyridones can inhibit at pharmacologically relevant concentrations the phosphatase activity of PTP4A3 independent of prominent ROS generation. While PTPs in general are suspectable to oxidation in vitro, a recent proteome-wide analysis of intracellular cysteine oxidation with exogenous H_2O_2 exposure did not show any evidence of PTP4A3 oxidation (van der Reest et al., 2018). Even if the iminothienopyridones produced ROS at very high concentrations, they could be potentially useful as at least 12 clinically used anticancer drugs have been shown to produce ROS (Yokoyama et al., 2017). This may be due in part to an altered redox homeostasis in cancer cells that preferentially sensitizes them to ROS (Yang et al., 2018). Recent work has highlighted the close integration of processes that regulate protein homeostasis and emphasize the unique dependence of cancer cells on thiols and deubiquitinases for survival (Harris et al., 2019). Loss of intracellular thiol-based reductants led to endoplasmic reticulum and proteotoxic stress and altered cancer cell sensitivity to therapeutic agents (Harris et al., 2019). Thus, the generation of intracellular ROS by compounds can

selectively alter cancer cell redox status. Collectively, therefore, our results should stimulate a further investigation of the pharmacological actions of the iminothienopyridone chemotype.

Acknowledgments

We are grateful for the assistance from the University of Virginia Advanced Microscopy Facility and the Bioinformatics Core. We thank Awais Paracha, who was supported by the Summer Undergraduate Research Fellow Award to the University of Virginia from the American Society for Pharmacology and Experimental Therapeutics, for his assistance with the initial ROS studies. We appreciate the cancer cell line data available from the Cancer Cell Line Encyclopedia.

Authors Contributions

Participated in the research design: Lazo, Wipf, Sharlow, Hsu

Conducted experiments: Blanco, Garrott, Hart, Tasker, Rastelli

Contributed new reagents or analytic tools: McCloud, Hsu, Burnett, Wipf

Performed data analysis: Hsu, McCloud, Blanco, Tasker, Rastelli, Burnett, Wipf

Wrote or contributed in the writing of the manuscript: Lazo, Wipf, Sharlow

References

Basak S, Jacobs SB, Krieg AJ, Pathak N, Zeng Q, Kaldis P, Giaccia AJ and Attardi LD (2008) The metastasis-associated gene prl-3 is a p53 target involved in cell-cycle regulation. *Mol Cell* **30**:303-314.

Bonham CA and Vacratsis PO (2009) Redox regulation of the human dual spcecificity phosphatase YVH1 through disulfide bond formation. *J Biol Chem* **284**:22853-22864.

Brisson M, Nguyen T, Wipf P, Joo B, Day BW, Skoko JS, Schreiber EM, Foster C, Bansal P and Lazo JS (2005) Redox regulation of CDC25b by cell-active quinolinediones. *Mol Pharmacol* **68**:1810-1820.

Buhrman G, Parker B, Sohn J, Rudolph J and Mattos C (2005) Structural mechanism of oxidative regulation of the phosphatase CDC25b via an intramolecular disulfide bond. *Biochemistry* **44**:5307-5316.

Chakraborty AA, Laukka T, Myllykoski M, Ringel AE, Booker MA, Tolstorukov MY, Meng YJ, Meier SR, Jennings RB, Creech AL, Herbert ZT, McBrayer SK, Olenchock BA, Jaffe JD, Haigis MC, Beroukhim R, Signoretti S, Koivunen P and Kaelin WG, Jr. (2019) Histone demethylase kdm6a directly senses oxygen to control chromatin and cell fate. *Science* **363**:1217-1222.

Daouti S, Li WH, Qian H, Huang KS, Holmgren J, Levin W, Reik L, McGady DL, Gillespie P, Perrotta A, Bian H, Reidhaar-Olson JF, Bliss SA, Olivier AR, Sergi JA, Fry D, Danho W, Ritland S, Fotouhi N, Heimbrook D and Niu H (2008) A selective phosphatase of regenerating liver

phosphatase inhibitor suppresses tumor cell anchorage-independent growth by a novel mechanism involving p130cas cleavage. *Cancer Res* **68**:1162-1169.

Defelipe LA, Lanzarotti E, Gauto D, Marti MA and Turjanski AG (2015) Protein topology determines cysteine oxidation fate: The case of sulfenyl amide formation among protein families. *PLoS Comput Biol* **11**:e1004051.

den Hollander P, Rawls K, Tsimelzon A, Shepherd J, Mazumdar A, Hill J, Fuqua SA, Chang JC, Osborne CK, Hilsenbeck SG, Mills GB and Brown PH (2016) Phosphatase PTP4A3 promotes triple-negative breast cancer growth and predicts poor patient survival. *Cancer Res* **76**:1942-1953.

Gasteiger E, Hoogland C, Gattiker A, Duvaud S, Wilkins MR, Appel RD and Bairoch A (2005) *Protein identification and analysis tools on the expasy server*. Humana Press.

Gulerez I, Funato Y, Wu H, Yang M, Kozlov G, Miki H and Gehring K (2016) Phosphocysteine in the PRL-CNNM pathway mediates magnesium homeostasis. *EMBO Rep* **17**:1890-1900.

Hardy S, Kostantin E, Hatzihristidis T, Zolotarov Y, Uetani N and Tremblay ML (2018) Physiological and oncogenic roles of the PRL phosphatases. *FEBS J* **285**:3886-3908.

Harris IS, Endress JE, Coloff JL, Selfors LM, McBrayer SK, Rosenbluth JM, Takahashi N, Dhakal S, Koduri V, Oser MG, Schauer NJ, Doherty LM, Hong AL, Kang YP, Younger ST, Doench JG, Hahn WC, Buhrlage SJ, DeNicola GM, Kaelin WG, Jr. and Brugge JS (2019)

Deubiquitinases maintain protein homeostasis and survival of cancer cells upon glutathione depletion. *Cell Metab* **29**:1166-1181.e1166.

Hoeger B, Diether M, Ballester PJ and Kohn M (2014) Biochemical evaluation of virtual screening methods reveals a cell-active inhibitor of the cancer-promoting phosphatases of regenerating liver. *Eur J Med Chem* **88**:89-100.

Hoeger B, Rios P, Berteotti A, Hoermann B, Duan G and Kohn M (2017) Mutational analysis of a conserved glutamate reveals unique mechanistic and structural features of the phosphatase PRL-3. *ACS Omega* **2**:9171-9180.

Ishii T, Funato Y and Miki H (2013) Thioredoxin-related protein 32 (TRP32) specifically reduces oxidized phosphatase of regenerating liver (PRL). *J Biol Chem* **288**:7263-7270.

Johnston PA (2011) Redox cycling compounds generate H2O2 in hts buffers containing strong reducing reagents--real hits or promiscuous artifacts? *Curr Opin Chem Biol* **15**:174-182.

Johnston PA, Soares KM, Shinde SN, Foster CA, Shun TY, Takyi HK, Wipf P and Lazo JS (2008) Development of a 384-well colorimetric assay to quantify hydrogen peroxide generated by the redox cycling of compounds in the presence of reducing agents. *Assay Drug Dev Technol* **6**:505-518.

Karantza V (2011) Keratins in health and cancer: More than mere epithelial cell markers. *Oncogene* **30**:127-138.

Kozlov G, Cheng J, Ziomek E, Banville D, Gehring K and Ekiel I (2004) Structural insights into molecular function of the metastasis-associated phosphatase PRL-3. *J Biol Chem* **279**:11882-11889.

Lazo JS and Sharlow ER (2016) Drugging undruggable molecular cancer targets. *Annu Rev Pharmacol Toxicol* **56**:23-40.

Lor LA, Schneck J, McNulty DE, Diaz E, Brandt M, Thrall SH and Schwartz B (2007) A simple assay for detection of small-molecule redox activity. *J Biomol Screen* **12**:881-890.

McParland V, Varsano G, Li X, Thornton J, Baby J, Aravind A, Meyer C, Pavic K, Rios P and Köhn M (2011) The metastasis-promoting phosphatase PRL-3 shows activity toward phosphoinositides. *Biochemistry* **50**:7579-7590.

McQueeney KE, Salamoun JM, Ahn JG, Pekic P, Blanco IK, Struckman HL, Sharlow ER, Wipf P and Lazo JS (2018) A chemical genetics approach identifies PTP4A3 as a regulator of colon cancer cell adhesion. *FASEB J* **32**:5661-5673.

McQueeney KE, Salamoun JM, Burnett JC, Barabutis N, Pekic P, Lewandowski SL, Llaneza DC, Cornelison R, Bai Y, Zhang ZY, Catravas JD, Landen CN, Wipf P, Lazo JS and Sharlow ER (2017) Targeting ovarian cancer and endothelium with an allosteric PTP4A3 phosphatase inhibitor. *Oncotarget* **9**:8223-8240.

Orsatti L, Innocenti F, Lo Surdo P, Talamo F and Barbato G (2009) Mass spectrometry study of PRL-3 phosphatase inactivation by disulfide bond formation and cysteine into glycine conversion. *Rapid Commun Mass Spectrom* **23**:2733-2740.

Pani G, Colavitti R, Bedogni B, Anzevino R, Borrello S and Galeotti T (2000) A redox signaling mechanism for density-dependent inhibition of cell growth. *J Biol Chem* **275**:38891-38899.

Rios P, Li X and Kohn M (2012) Molecular mechanisms of the PRL phosphatases. *FEBS J* **280**:505-524.

Salamoun JM, McQueeney KE, Patil K, Geib SJ, Sharlow ER, Lazo JS and Wipf P (2016) Photooxygenation of an amino-thienopyridone yields a more potent PTP4A3 inhibitor. *Org Biomol Chem* **14**:6398-6402.

Schieber M and Chandel N (2014) Ros function in redox signaling and oxidative stress. *Curr Biol* **24**:R453-R462.

Soares KM, Blackmon N, Shun TY, Shinde SN, Takyi HK, Wipf P, Lazo JS and Johnston PA (2010) Profiling the nih small molecule repository for compounds that generate H2O2 by redox cycling in reducing environments. *Assay Drug Dev Technol* **8**:152-174.

Stadlbauer S, Rios P, Ohmori K, Suzuki K and Kohn M (2015) Procyanidins negatively affect the activity of the phosphatases of regenerating liver. *PLoS One* **10**:e0134336.

Stanford SM and Biottini N (2017) Targeting tyrosine phosphatases: Time to end the stigma. *Trends Pharmacol Sci* **38**:524-540.

Tanner JJ, Parsons ZD, Cummings AH, Zhoi H and Gates KS (2011) Redox regulation of protein tyrosine phosphatases: Structural and chemical aspects. *Antioxid Redox Signal* **15**:77-97.

Tasker NK, Rastelli EJ, Blanco IK, Sharlow ER, Lazo JS and Wipf P (2019) In-flow photooxygenation of aminothienopyridinones generates iminopyridinedione PTP4A3 phosphatase inhibitors. *Org Biomol Chem* **17**:2448-2466.

van der Reest J, Lilla S, Zheng L, Zanivan S and Gottlieb E (2018) Proteome-wide analysis of cysteine oxidation reveals metabolic sensitivity to redox stress. *Nat Commun* **9**:1581.

Vogt A, McDonald PR, Tamewitz A, Sikorski RP, Wipf P, Skoko JJ, 3rd and Lazo JS (2008) A cell-active inhibitor of mitogen-activated protein kinase phosphatases restores paclitaxel-induced apoptosis in dexamethasone-protected cancer cells. *Mol Cancer Ther* **7**:330-340.

Wang H, Quah SY, Dong JM, Manser E, Tang JP and Zeng Q (2007) PRL-3 down-regulates pten expression and signals through pi3k to promote epithelial-mesenchymal transition. *Cancer Res* **67**:2922-2926.

Wisniewski JR, Zougman A, Nagaraj N and Mann M (2009) Universal sample preparation method for proteome analysis. *Nat Protocol* **6**:359-362.

Yang H, Villani RM, Wang H, Simpson MJ, Roberts MS, Tang M and Liang X (2018) The role of cellular reactive oxygen species in cancer chemotherapy. *J Exp Clin Cancer Res* **37**:266.

Yokoyama C, Sueyoshi Y, Ema M, Mori Y, Takaishi K and Hisatomi H (2017) Induction of oxidative stress by anticancer drugs in the presence and absence of cells. *Oncol Lett* **14**:6066-6070.

Yu ZH and Zhang ZY (2017) Regulatory mechanisms and novel therapeutic targeting stragegies for protein tyrosine phosphatases. *Chem Rev* **50**:122-129.

Zhang H, Kozlov G, Li X, Wu H, Gulerez I and Gehring K (2017) PRL3 phosphatase active site is required for binding the putative magnesium transporter cnnm3. *Sci Rep* **7**:48.

Zhang Z, Kozlov G, Chen YS and Gehring K (2019) Mechanism of thienopyridone and iminothienopyridinedione inhibition of protein phosphatases. *MedChemComm* **10**:791-799.

Footnotes

*The work was supported by grants from the Department of Defense [W81XWH-18-1-0012], the National Institutes of Health [S10 OD021723], the Fiske Drug Discovery Fund, the Owens Foundation, and the Ivy Foundation. This material is based upon work supported by the National Science Foundation Graduate Research Fellowship Program [Grant No. 2018255830]. Any opinions, findings, and conclusions or recommendations expressed in this material are those of the authors and do not necessarily reflect the views of the National Science Foundation. This article is dedicated to the memory of Nancy Ann Lazo Higgins, who courageously fought her ovarian cancer.

Address correspondence to: John S. Lazo, Department of Pharmacology, Fiske Drug Discovery Laboratory, P.O. Box 800735, University of Virginia, Charlottesville, VA 22908-0735; Telephone: 434-243-1936; Fax: 434-982-0874; Email: lazo@virginia.edu

JPET Fast Forward. Published on October 10, 2019 as DOI: 10.1124/jpet.119.262188
This article has not been copyedited and formatted. The final version may differ from this version.

Legends for the Figures

Figure 1. Chemical structures of the thienopyridone analogs.

Figure 2. Small molecule inhibitor PTP4A1, PTP4A2, and PTP4A3 concentration-response curves and reversibility studies. PTP4A family inhibition. Panel A. JMS-053. Panel B. EJR-866-75. Panel C. EJR-866-81. Panel D. NRT-870-59. Panel E. JMS-038. Black symbols, PTP4A3; blue symbols, PTP4A1; red symbols, PTP4A2. Panel F. Reversible PTP4A3 inhibition by NRT-870-59. Full length recombinant PTP4A3 was treated with a concentration of NRT-870-59 equal to the IC_{50} or 10-fold higher, namely 86 or 860 nM, respectively. A pre-incubated (Pre-I) sample was exposed to a concentration of NRT-870-59 that was 10-fold higher than the IC_{50} for 30 min and then diluted to 86 nM. Enz, enzyme. N=3. Bars = SEM unless smaller than the symbol.

Figure 3. Redox activity of JMS-053 analogs and pre-incubation studies with JMS-053. Panel A. Detection of ROS using resazurin in the presence of DTT. Panel B. Detection of ROS using a phenol red-horseradish peroxidase assay in the presence of DTT. ● - DA-3003-1; ■ - JMS-053; ▲ - JMS-038; ▼ - EJR-866-75; ♦ - NRT-870-59; ● - EJR-866-81. Panel C. Preincubation of PTP4A3 with JMS-053 for 2 h prior to addition of substrate. Black symbols are with no pre-incubation and red symbols are with a 2 h pre-incubation. Bars = SEM, N = 3.

Figure 4. Panel A. Base peak chromatograms of WT PTP4A3 tryptic peptides after treatment of the protein with JMS-053. A comparison was made between samples that were treated with DTT to reduce disulfide bonds before alkylation with IAA, and those that received only IAA treatment. PTP4A3 contains two tryptic peptides with Cys. While little to no change was observed in the peptide containing C49 (*m/z*=507.4), the second Cys containing peptide

(*m/z*=683.7) disappeared in the absence of DTT. A new peak for this peptide was found with an *m/z*=645.0 corresponding to a single alkylation of C93. No additional peaks were found to indicate the formation of a disulfide bond. Panel B. Base peaks for Cys containing peptides at *m/z*=507.4, *m/z*=683.7, and *m/z*=645.0. The single Cys on peptide VCEVTYDK allowed for quick interpretation for the presence of possible disulfide bonds at C49 by measuring their relative abundances between reduced v. non-reduced samples. No significant change was found in this peptide's relative abundance. In the absence of DTT, the peak found at *m/z*=645.0 contributed significantly to the relative abundance of the second peptide of interest with a single alkylation. A second peak was found with a retention time ~21.2 min and is likely a structural isomer of the peptide with an alkylation on the other cysteine residues. The sum of these peaks account for a majority of the FCEAPGSCVAVHCVAGLGR peptide. Panel C. MS2 fragment spectra of *m/z* 507.4. y and b ion coverage of provide the amino acid sequence of VC(+57.02)EVTYDK and confirm the identity of the peptide found in both reduced and non-reduced samples.

Figure 5. Inhibition of colony formation, lack of intracellular reactive oxygen species generation, and gene expression profiling. Panel A. Mouse colon cancer cells (white columns) and an isogenic PTP4A3 null cell line (gray columns) were expose to NRT-870-59, JMS-038 or vehicle and colony formation determined after a two-week incubation. Mean value from three wells and error bars = SEM. Representative of two independent assays with similar results. N=3. * = $p<0.05$. Error bars = SEM. NS = difference not statistically significant. Panel B. Formation of ROS was determined in confluent OVCAR4 ovarian cancer cells using the ROS-Glo H_2O_2 assay. N=3. * = $p<0.05$. Error bars = SEM. Panel C. Commonly altered pathways in PTP4A3 wildtype and null cells and the JMS-053 treated PTP4A3 wildtype cells.

JPET Fast Forward. Published on October 10, 2019 as DOI: 10.1124/jpet.119.262188
This article has not been copyedited and formatted. The final version may differ from this version.

Table 1. IC_{50} values for PTP4A3 inhibitors.

	Mean (nM) ± SEM								
Compound	PTP4A1	PTP4A2	PTP4A3	PTP4A3 C49S	PTP4A3 K144I	PTP4A3 A106V	PTP4A3 A111S	CDC25B	DUSP3
JMS-053	29.1 ± 2.7	48.0 ± 14.5	34.7 ± 2.5[a]	156.5 ± 20.1[f]	42.7 ± 8.0	26.3 ± 2.5	104.4 ± 7.7[*e]	92.6 ± 10.2[f]	207.6 ± 46.3
EJR-866-81	49.0 ± 5.0	112.9* ± 10.0	36.1 ± 1.4	390.0 ± 72.5[f]	59.1 ± 5.9	54.5 ± 2.4	61.0 ± 2.8[*e]	65.5 ± 16.6[f]	240.8 ± 30.9
EJR-866-75	43.2 ± 8.5	73.9 ± 10.0	98.2 ± 2.5[b]	229.7* ± 54.6	68.5 ± 1.0	57.5 ± 18.6	172.0 ± 46.0[e,f]	122.6 ± 22.6	521.0 ± 128.4
NRT-870-59[b]	133.2 ± 31.7[a]	264.4[f] ± 37.4[a]	86.0 ± 12.6[a]	332.2[f] ± 52.5	180.2 ± 64.5[c]	57.7 ± 18.6	>1,000[e]	>1,000	411.8 ± 75.3
JMS-038	>1,000	>1,000	>1,000	ND	>1,000	ND	ND	ND	> 1,000

The in vitro IC_{50} values for the iminopyridinediones was determined with recombinant human protein using the artificial substrate DiFMUP, an automated liquid handling platform and a 25 min incubation. N=3 independent experiments unless marked: [a]N=8, [b]N=6, [c]N=5, [d]N=4, or [e]N=2. ND = not determined. [f]$p<0.05$ compared to PTP4A3.

JPET Fast Forward. Published on October 10, 2019 as DOI: 10.1124/jpet.119.262188
This article has not been copyedited and formatted. The final version may differ from this version.

Table 2. Kinetic determinations for wildtype and mutant forms of PTP4A3.

	PTP4A3	**PTP4A3 C49S**	**PTP4A3 K144I**	**PTP4A3 A106V**	**PTP4A3 A111S**
K_m (μM)	4.04 ± 0.59	41.10 ± 9.01	4.73 ± 0.71	32.04 ± 6.88	18.94 ± 6.16
K_{cat} (min^{-1})	5.77 ± 0.53	4.93 ± 0.24	6.47 ± 0.69	8.51 ± 2.14	38.72 ± 6.78
K_{cat}/K_m ($min^{-1}\mu M^{-1}$)	1.50 ± 0.53	0.13 ± 0.03	1.40 ± 0.24	0.26 ± 0.01	2.21 ± 0.46

The kinetic parameters were determined with wild type and mutant forms of recombinant human PTP4A3 and the artificial substrate DiFMUP. N=3, mean ± SEM.

JPET Fast Forward. Published on October 10, 2019 as DOI: 10.1124/jpet.119.262188
This article has not been copyedited and formatted. The final version may differ from this version.

Table 3. Cellular IC_{50} values for loss of spheroid viability after a 48 h exposure.

	μM ± SEM			
	MDA-MB-231	Hs578T	OVCAR4	Kuramochi
JMS-053	32.67 ± 7.02	8.48 ± 2.38	4.42 ± 1.04	13.25 ± 0.65
EJR-866-75	> 50 μM	12.01 ± 3.84	19.64 ± 4.66[a]	> 50 μM
EJR-866-81	> 50 μM	14.39 ± 4.91	12.35 ± 2.26[a]	> 50 μM
NRT-870-59	61.54 ±9.66[a]	10.07 ± 1.93	11.50 ± 2.38[a]	34.14 ± 8.60[a]
JMS-038	>50 μM	>50 μM	>50 μM	>50 μM

Exponentially growing human breast and ovarian cancer cells were plated in ultralow attachment U-bottom microtiter plates, cultured for 24 h to allow spheroid formation. Compounds were added to the pre-existing spheroids and microtiter plates were incubated for 48 h. Cell viability was determined with CellTiterGlo. N=3, mean ± SEM. [a] $p<0.05$ compared to JMS-053.

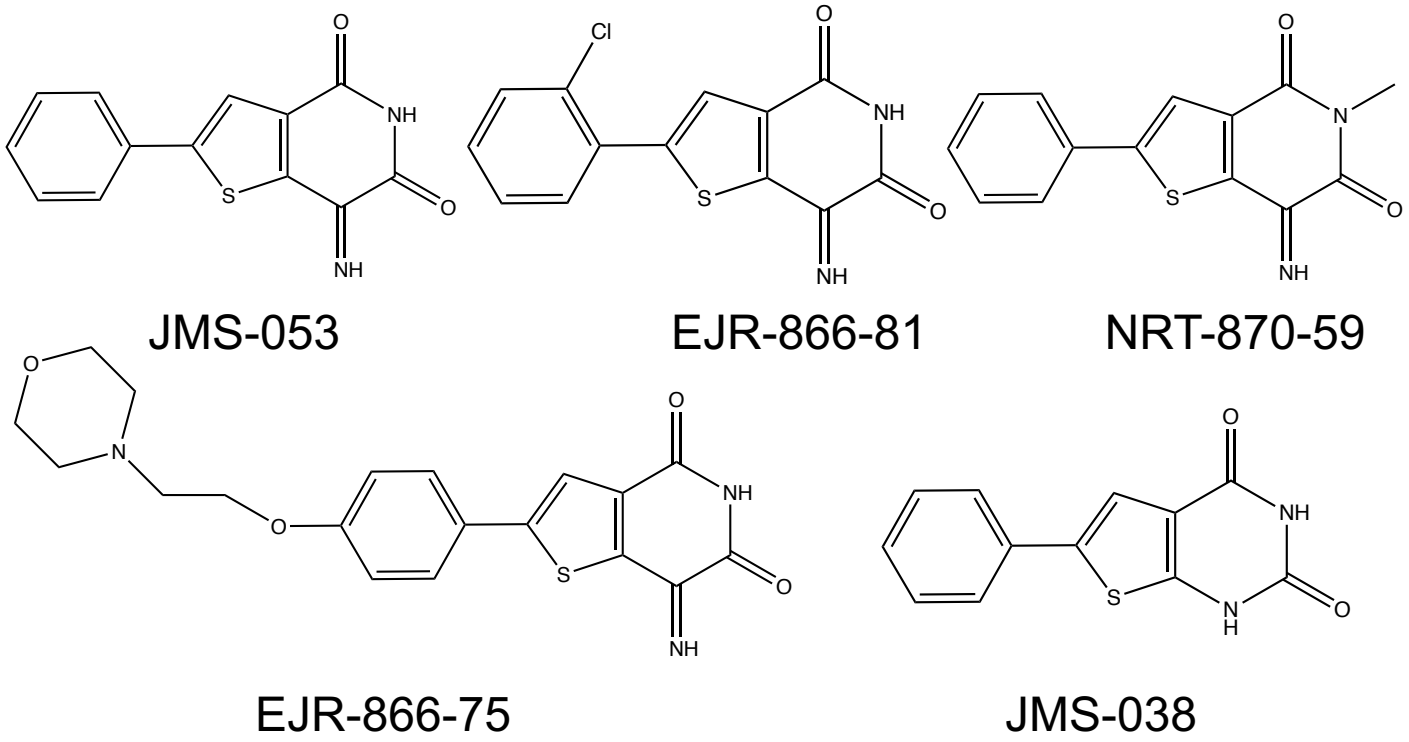

Figure 1

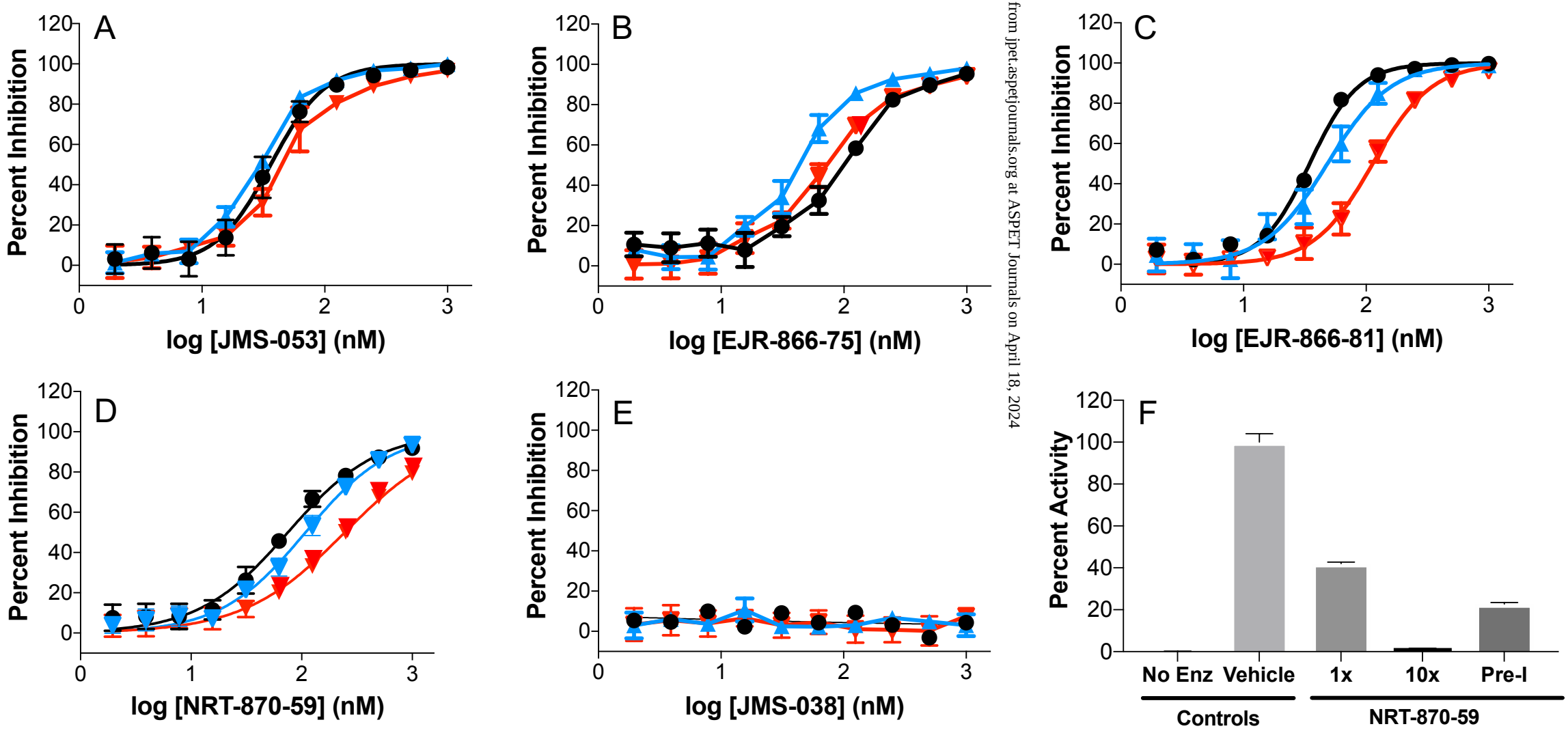

Figure 2

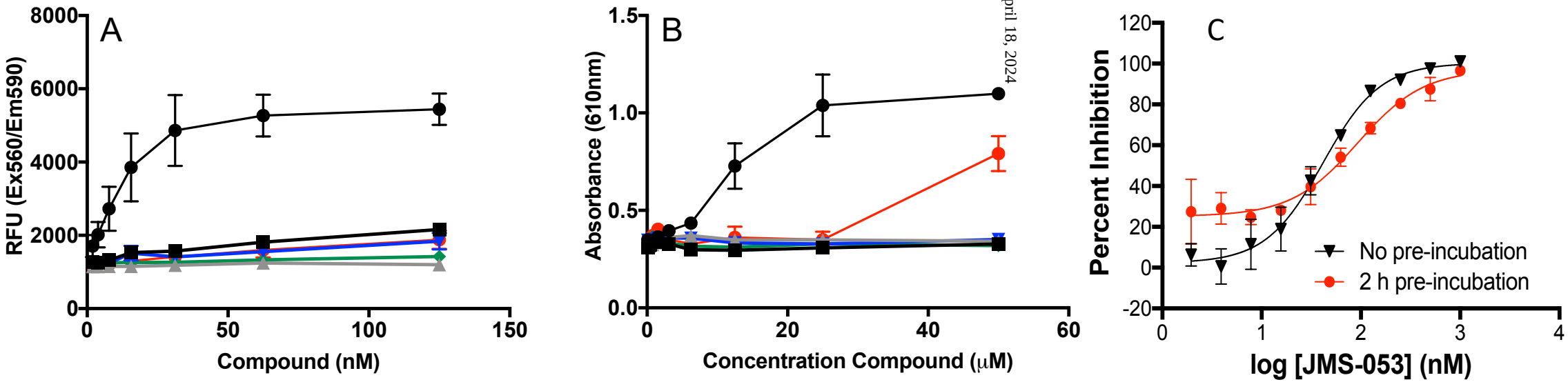

Figure 3

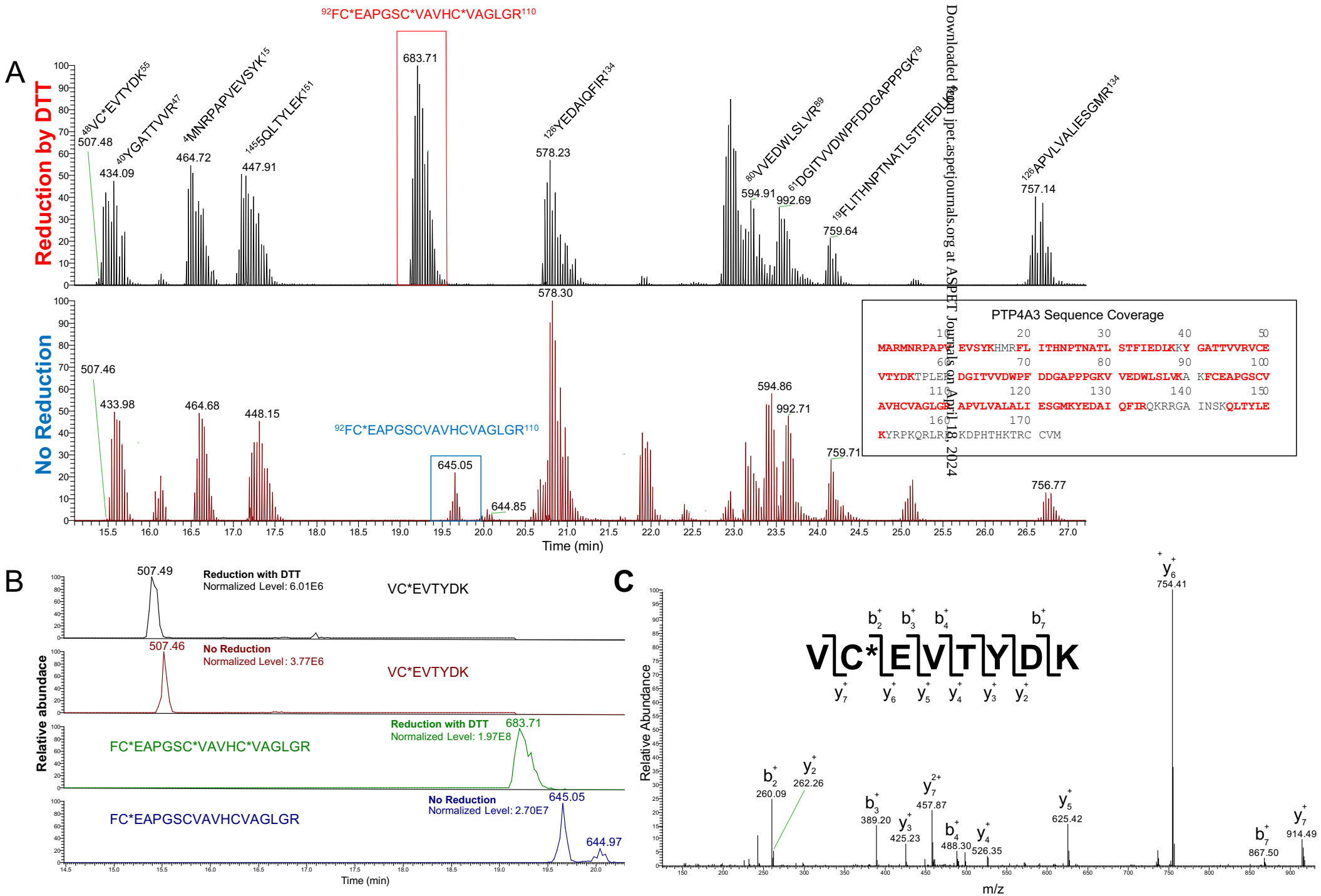
A
Reduction by DTT
92FC*EAPGSC*VAVHC*VAGLGR110
683.71
48VC*EVTYDK55
507.48
40YGATTVVR47
434.09
4MNRPAPVEVSYK15
464.72
1455QLTYLEK151
447.91
126YEDAIQFIR134
578.23
80VVEDWLSLVR89
594.91
61DGITVVDWPFDDGAPPPGK79
992.69
19FLITHNPTNATLSTFIEDLK39
759.64
126APVLVALIESGMR134
757.14
No Reduction
578.30
507.46
433.98
464.68
448.15
92FC*EAPGSCVAVHCVAGLGR110
645.05
644.85
594.86
992.71
759.71
756.77
Time (min)
PTP4A3 Sequence Coverage
MARMNRPAPVEVSYKHMRFLITHNPTNATLSTFIEDLKKYDGATTVVRVCE
VTYDKTPLEVDGITVVDWPFDDGAPPPGKVVEDWLSLVKAKFCEAPGSCV
AVHCVAGLGRAPVLVALALIESGMKYEDAIQFIRQKRRGAINSKQLTYLE
KYRPKQRLRLKDPHTHKTRCCVM
Downloaded from jpet.aspetjournals.org at ASPET Journals on April 16, 2024
B
Reduction with DTT
Normalized Level: 6.01E6
507.49
VC*EVTYDK
No Reduction
Normalized Level: 3.77E6
507.46
VC*EVTYDK
Reduction with DTT
Normalized Level: 1.97E8
683.71
FC*EAPGSC*VAVHC*VAGLGR
No Reduction
Normalized Level: 2.70E7
645.05
644.97
FC*EAPGSCVAVHCVAGLGR
Relative abundace
Time (min)
C
Relative Abundance
m/z
VC*EVTYDK
b2+ b3+ b4+ b7+
y7+ y6+ y5+ y4+ y3+ y2+
y6+ 754.41
b2+ 260.09
y2+ 262.26
b3+ 389.20
y3+ 425.23
y7 2+ 457.87
b4+ 488.30
y4+ 526.35
y5+ 625.42
b7+ 867.50
y7+ 914.49

Figure 4

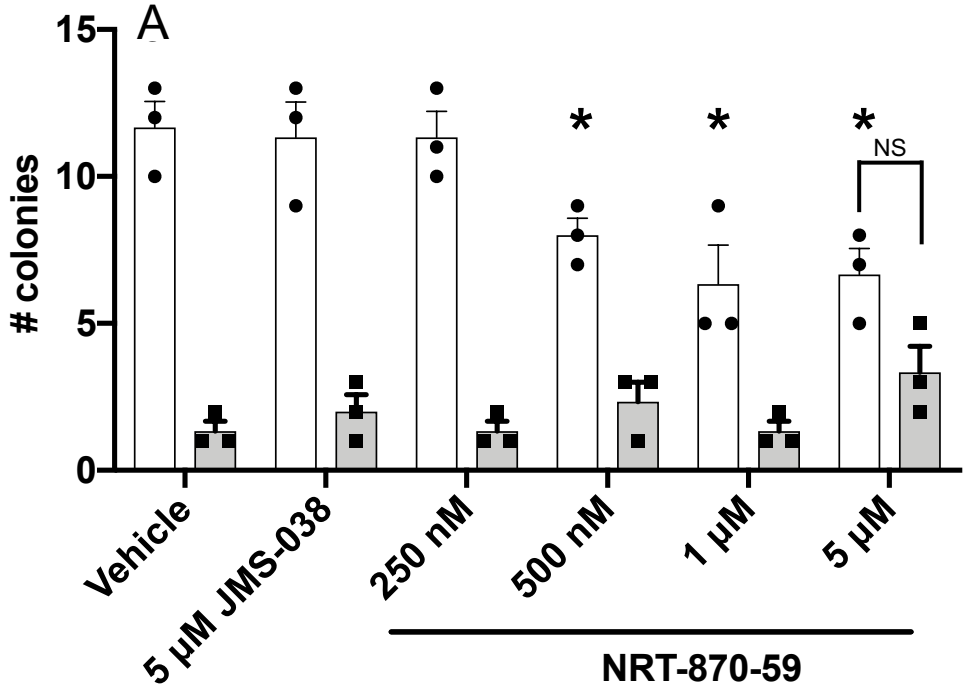

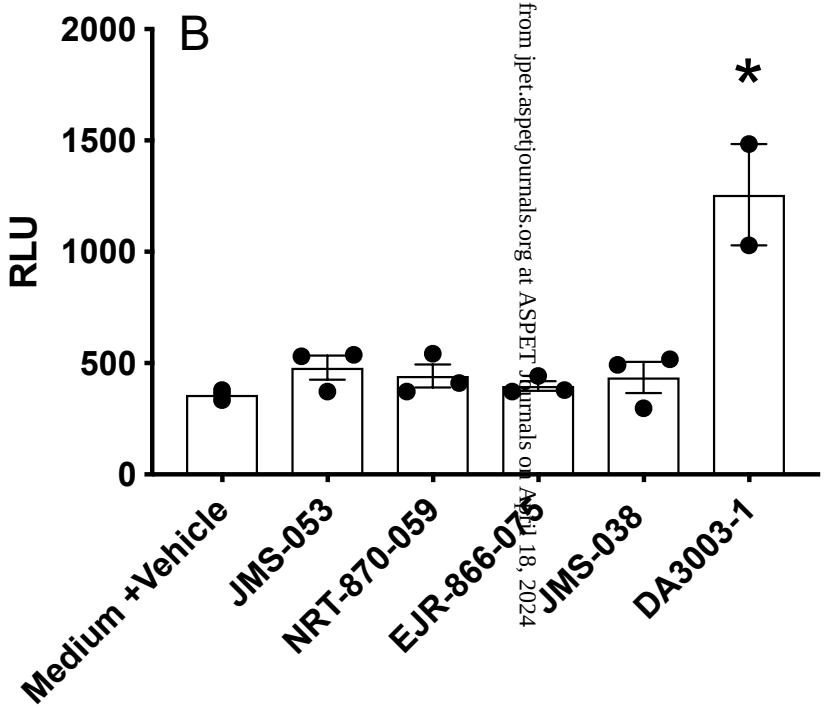

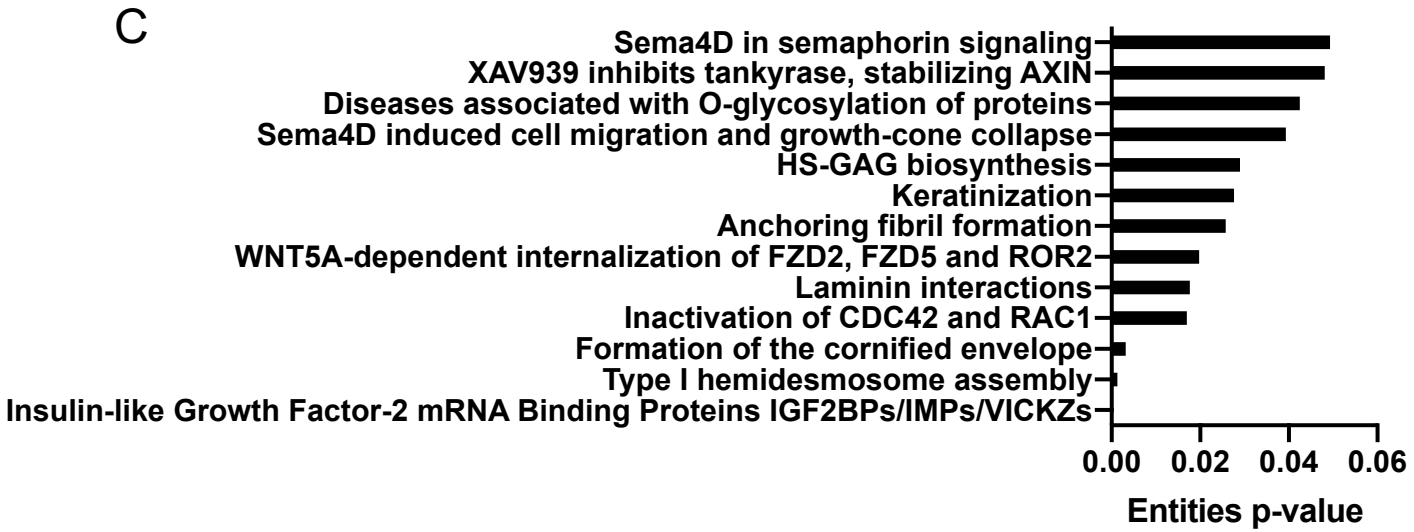

Figure 5

Supplemental Data JPET #262188

Next-Generation Cell-active Inhibitors of the Undrugged Oncogenic PTP4A3 Phosphatase*

John S. Lazo, Isabella K. Blanco, Nikhil R. Tasker, Ettore J. Rastelli, James C. Burnett, Sharon R. Garrott, Duncan J. Hart, Rebecca L. McCloud, Ku-Lung Hsu, Peter Wipf, and Elizabeth R. Sharlow

Department of Pharmacology (J.S.L., I.K.B., S.R.G., D.J.H., E.R.S.) and Chemistry (J.S.L., R.L.M., K-L.H.), University of Virginia, Charlottesville, VA; Department of Chemistry (N.R.T.,E.J.R., J.C.B., P.W.), University of Pittsburgh, Pittsburgh, PA

Supplemental Table 1. Mutations in breast and ovarian cancer cell lines

Cell Type	TP53	HRAS	KRAS	IL6R
MDA-MB-231	R280K	NR	G13D	NR
Hs578T	V157F	G13D	NR	NR
OVCAR4	L130V	NR	NR	NR
Kuramochi	D281Y	NR	NR	P431L

These data were obtained from the Cancer Cell Line Encyclopedia (https://portals.broadinstitute.org/ccle) dated September 2019. NR = none recorded.

Supplemental Figures

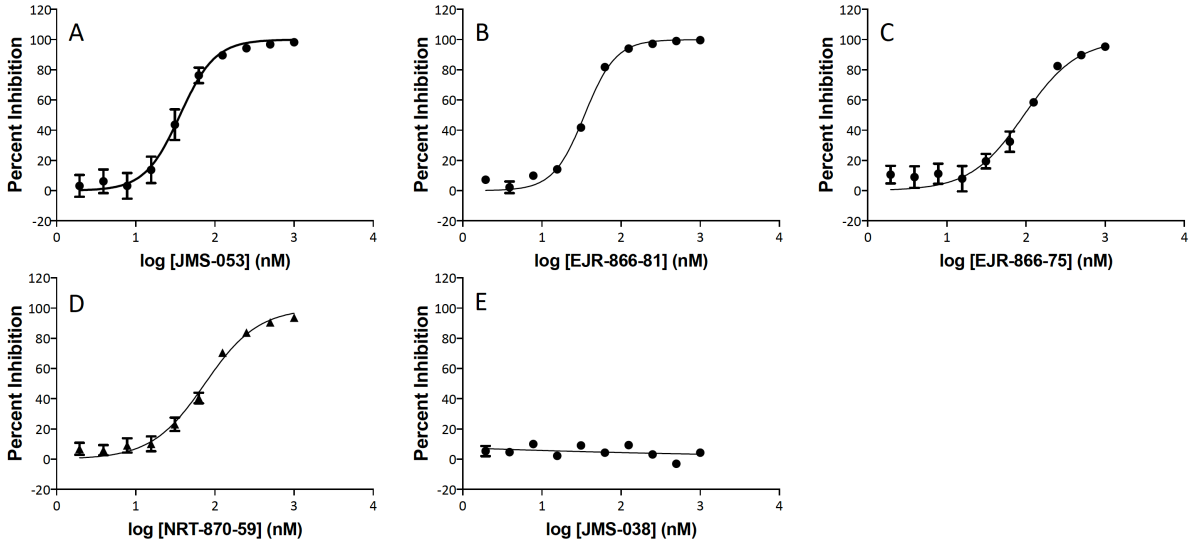

Supplemental Figure 1. Small molecule inhibitor PTP4A3 concentration-response curves. Panel A. JMS-053. Panel B. EJR-866-81. Panel C. EJR-866-75. Panel D. NRT-870-59. Panel E. JMS-038. N=3. Bars = SEM unless smaller than the symbol.

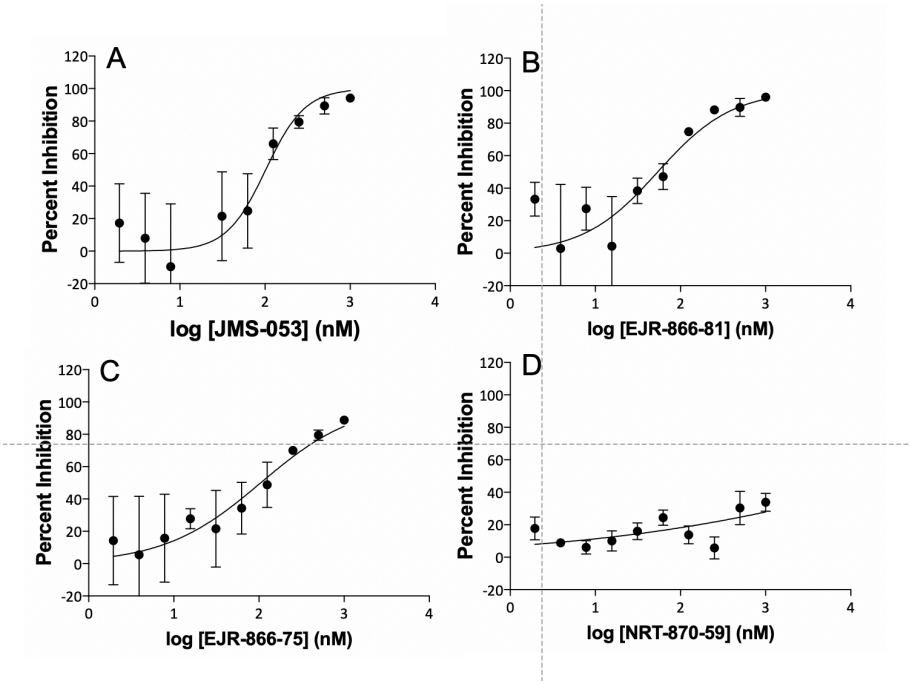

Supplemental Figure 2. CDC25B concentration-response curves. Panel A. JMS-053. Panel B. EJR-866-81. Panel C. EJR-866-75. Panel D. NRT-870-59. N=3. Bars = SEM unless smaller than the symbol.

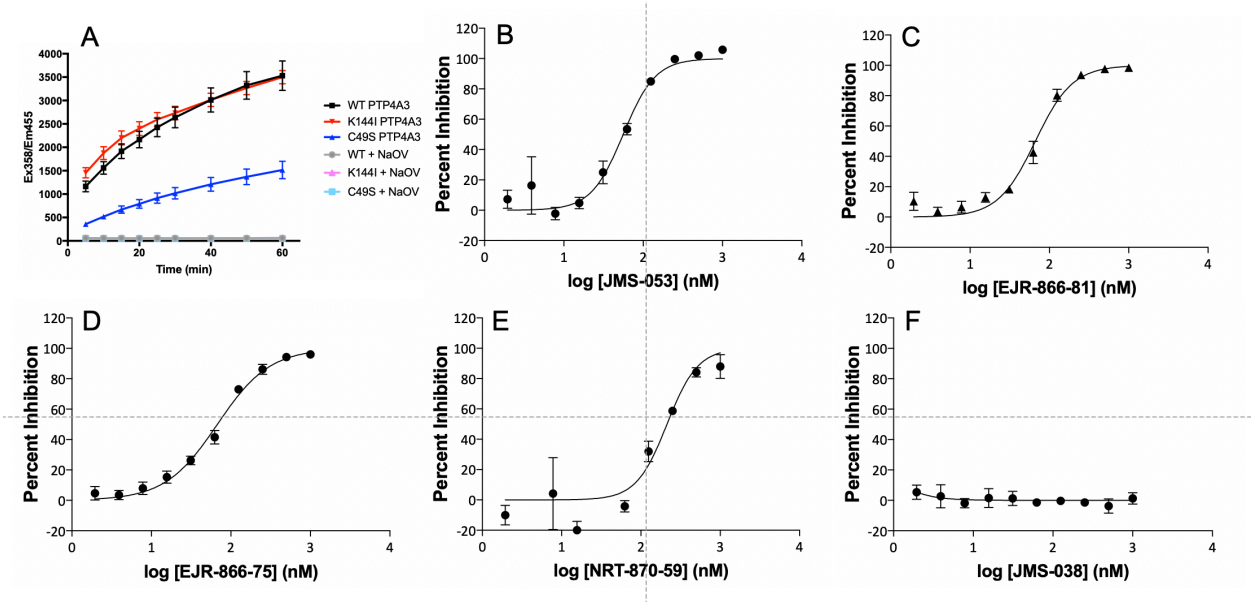

Supplemental Figure 3. Mutant enzymatic activity and PTP4A3 K144I mutant analog concentration response curves. Panel A. Enzymatic activity of PTP4A3 mutants and sensitivity to NaOV. ■ - wildtype PTP4A3; ▼ - K144I PTP4A3; ▲ - C49S PTP4A3; ● - wildtype PTP4A3 with NaOV; △ - K144I PTP4A3 with NaOV; □ - C49S PTP4A3 with NaOV. Panel B. JMS-053 inhibition of PTP4A3 K144I. Panel C. EJR-866-81 inhibition of PTP4A3 K144I. Panel D. EJR-866-75 inhibition of PTP4A3 K144I. Panel E. NRT-870-59 inhibition of PTP4A3 K144I. Panel F. JMS-038 lack of inhibition of PTP4A3 K144I. N=3. Bars = SEM unless smaller than the symbol.

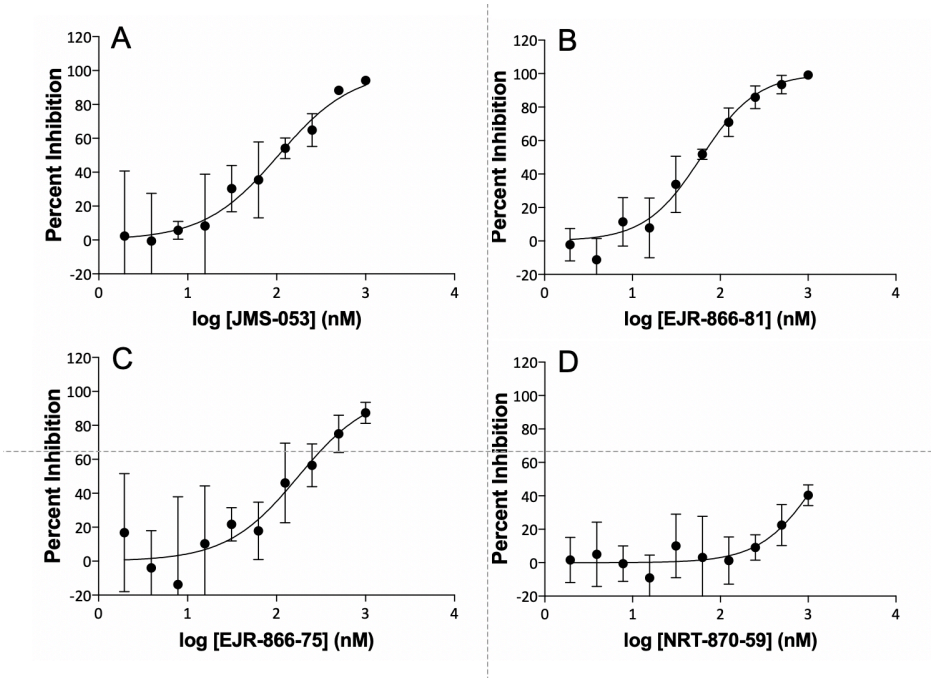

Supplemental Figure 4. PTP4A3 A111S mutant concentration-response curves. Panel A. JMS-053. Panel B. EJR-866-81. Panel C. EJR-866-75. Panel D. NRT-870-59. N=2. Bars = range unless smaller than the symbol.

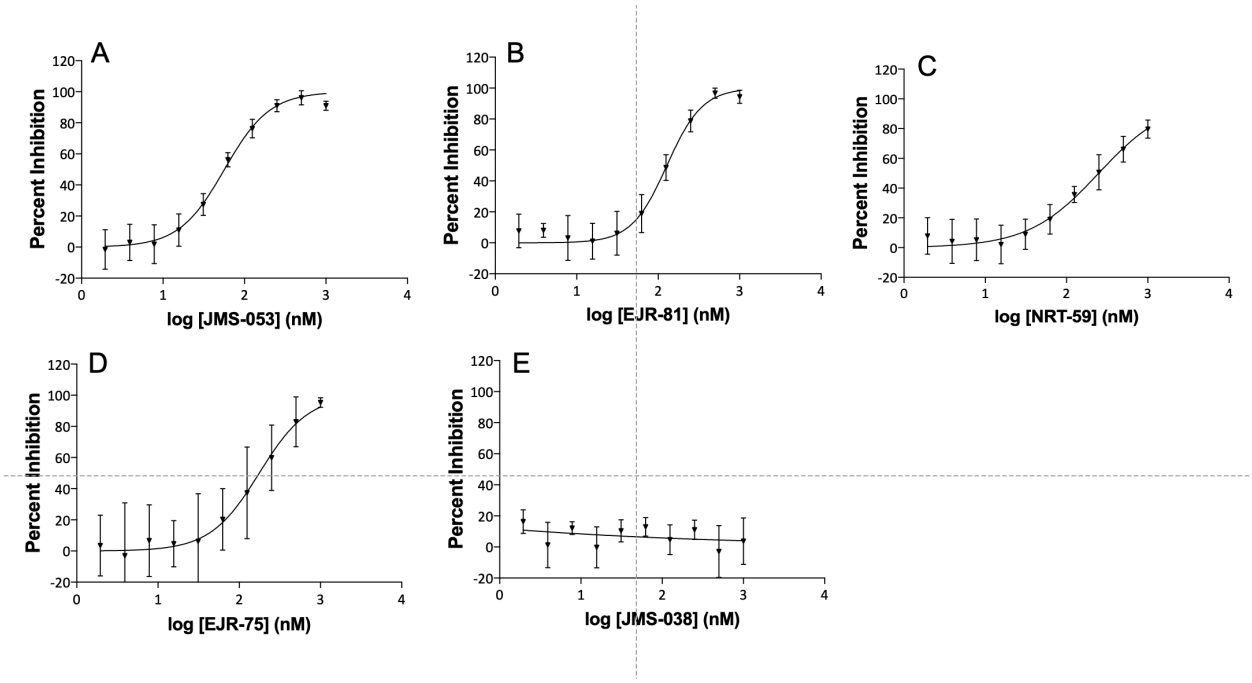

Supplemental Figure 5. C49S PTP4A3 concentration-response curves. Panel A. JMS-053. Panel B. EJR-866-81. Panel C. EJR-866-75. Panel D. NRT-870-59. Panel E. JMS-038. N=3. Bars = SEM unless smaller than the symbol.

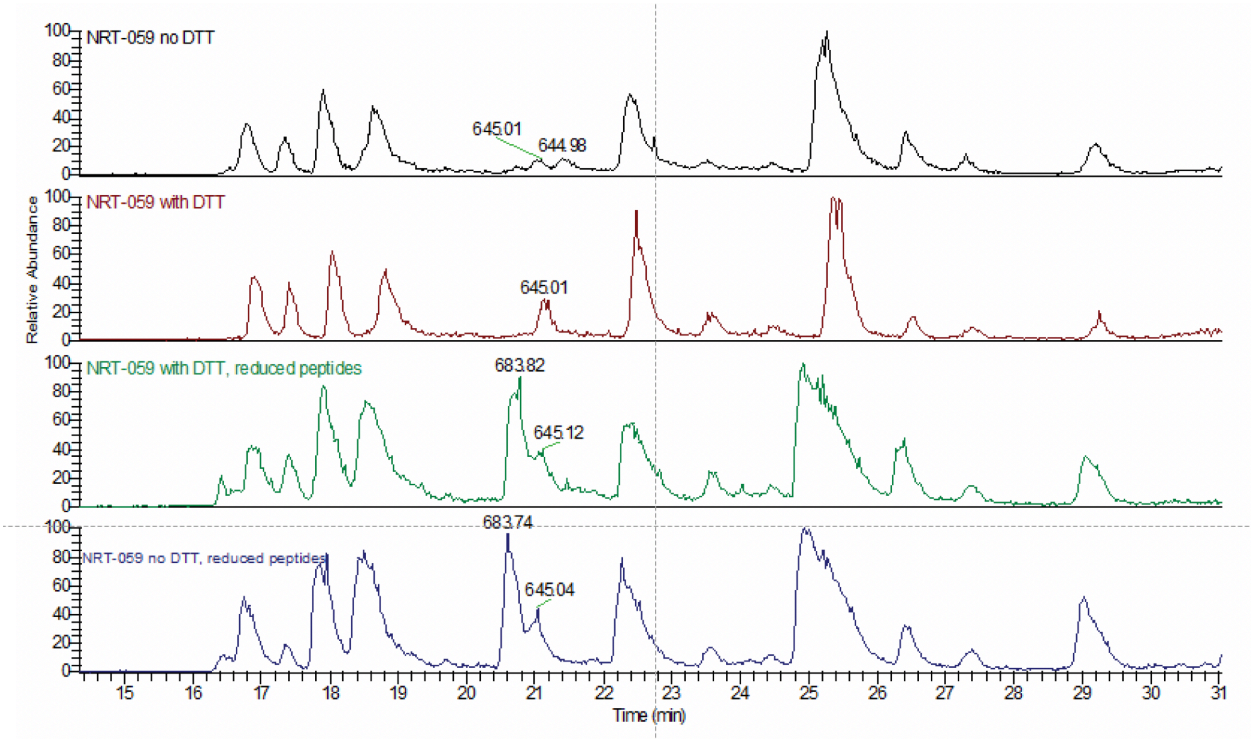

Supplemental Figure 6. PTP4A3 treatment with NRT-059 in reducing and non-reducing conditions. After treatment, half the samples were subject to additional reduction and alkylation with iodoacetamide, while the other half only received

iodoacetamide treatment. MS1 peaks of a mass between 644.90-645.10 were found once again for the peptide containing the catalytic cysteine residue, and no additional peaks were found to indicate a disulfide bond between C49 and C104.

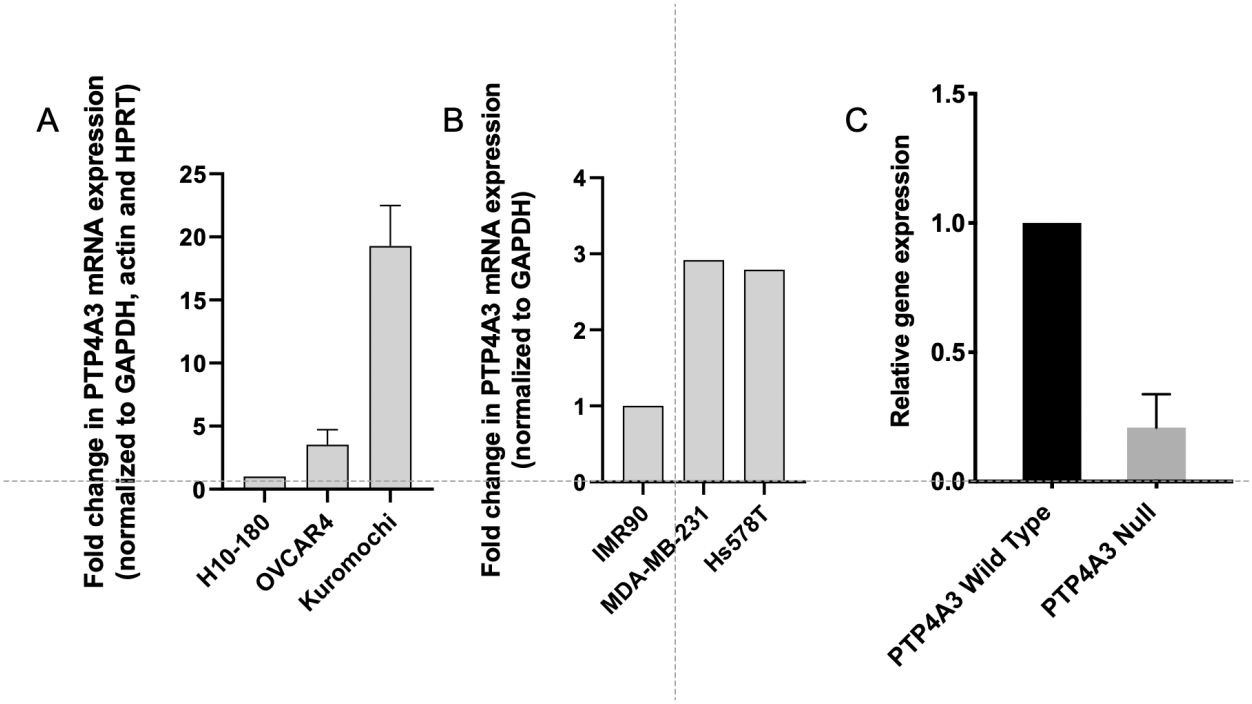

Supplemental Figure 7. Expression of PTP4A3 in human and murine cancer cells. PTP4A3 expression was determined by real-time quantitative polymerase chain reaction and normalized to GAPDH, actin and HPRT for human cells and HPRT for murine cells. Panel A. PTP4A3 mRNA levels in nonmalignant human ovarian epithelial H10-180 cells, OVACR4 and Kuramochi ovarian cancer cells. N=3-15 samples; bars = SEM. Panel B. PTP4A3 mRNA levels in nonmalignant human IMR90 fibroblasts. N=1. Panel C. PTP4A3 mRNA levels in mouse PTP4A3 wild type and null cells. N=2, bar = range.

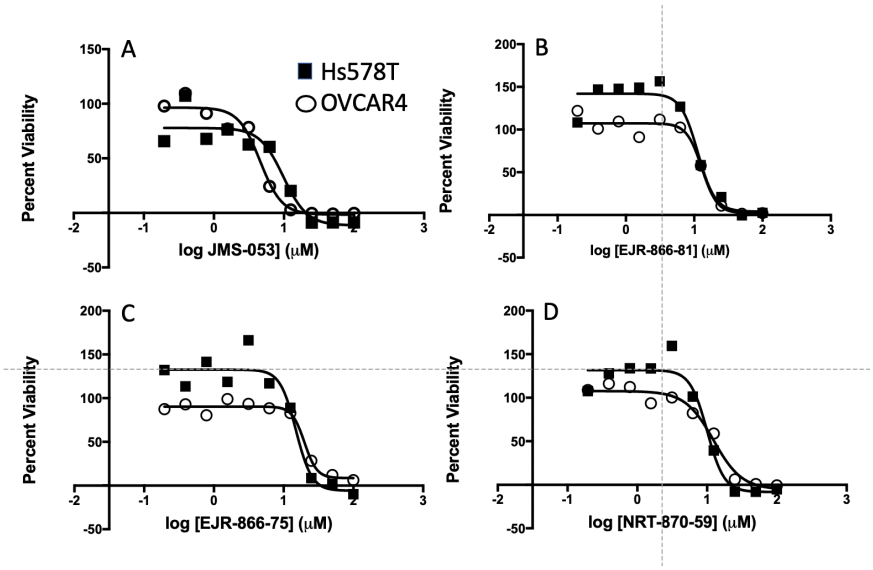

Supplemental Figure 8. Cytotoxicity of analogs to breast and ovarian cancer 72 h spheroid assay summary. Hs578T (□) and OVCAR4 (○). Panel A. JMS-053. Panel B. EJR-866-81. Panel C. EJR-866-75. Panel D. NRT-870-59.

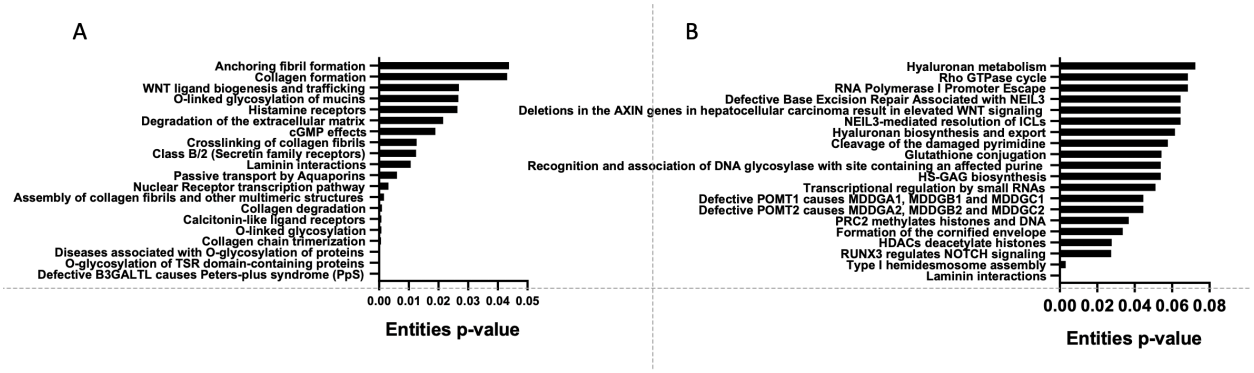

Supplemental Figure 9. Gene expression pathway analyses of mouse colon cancer cells after gene deletion or PTP4A3 inhibition. Panel A. Reactome pathway analysis of the mRNA transcripts over- or under-expressed in mouse colon cancer cells that contained or lacked PTP4A3. Panel B. Reactome pathway analysis of the mRNA transcripts over- or under-expressed in mouse colon cancer cells treated with vehicle or 1 μM JMS-053 for 24 h.